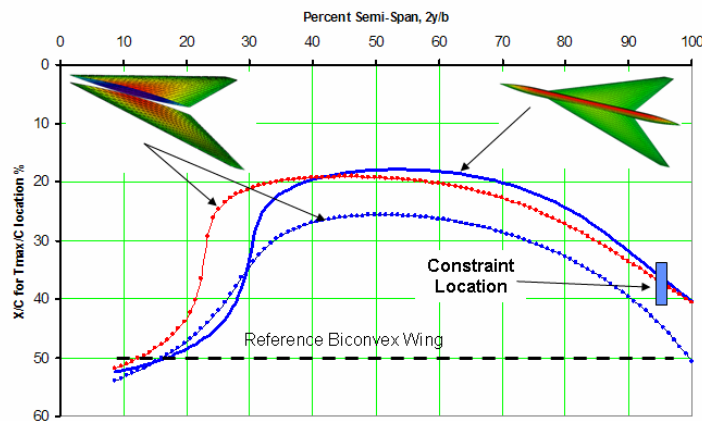
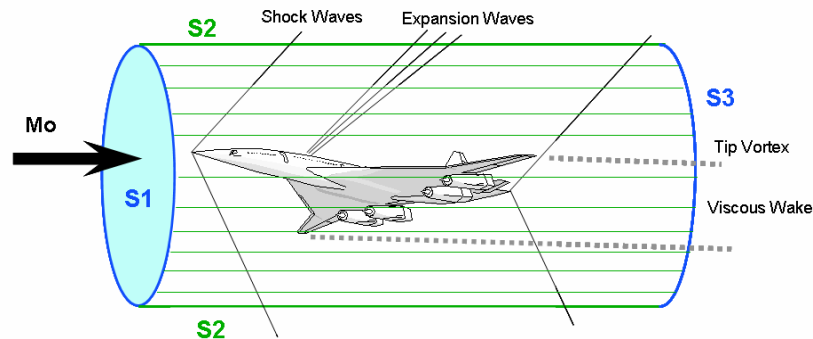


AIAA-2008-0132

A New Supersonic Wing Far-Field Composite Element Wave Drag Optimization Method, "FCE"

Brenda M. Kulfan

Boeing Commercial Airplanes, Seattle, Washington, 98124



46th AIAA Aerospace Sciences Meeting and Exhibit

7-10 January 2008

**Reno Hilton
Reno, Nevada**

A New Supersonic Wing Far-Field Composite Element Wave Drag Optimization Method, “FCE”

Brenda Kulfan¹

Boeing Commercial Airplanes, Seattle, Washington, 98124

NASA and Industry, recently ended the High Speed Civil Transport, HSCT, program. The objective of the HSCT program was to develop critical technologies to support the potential development of viable supersonic commercial transport aircraft. The initial phases of the HSCT program utilized the extensive database of methods and knowledge and expertise from the US Supersonic Transport, SST, program and the subsequent NASA sponsored Supersonic Cruise Research, SCR, studies. The aerodynamic design development activities benefited greatly from the use of the prior design, analysis and prediction methods as well as the understanding of the fundamental physics inherent in an efficient supersonic aircraft design. The emerging advanced Computational Fluid Dynamic methods greatly enhanced the supersonic design and analysis process and enabled substantial improvements in achievable aerodynamic performance levels. It was recognized that the critical strengths of the aerodynamic processes included the blending of the computational power offered by CFD methods with the fundamental knowledge and rapid design development and assessment capabilities inherent in the existing linear aerodynamic theory methods. Non-linear design optimization studies are typically initiated with an initial optimized linear theory baseline configuration design. In this paper a new supersonic linear theory wave drag optimization methodology utilizing far field wave drag methodology is introduced. The method is developed utilizing the Class Function / Shape Function Transformation, CST, concept of an analytic scalar wing definition. Comparisons are made with an optimized wing design with an optimized wing design that was developed and validated in the wind tunnel during the US SST program. The new methodology is then applied to an arrow wing planform to illustrate the versatility of the new optimization methodology as well as to demonstrate the usefulness of the CST analytic wing concept for aerodynamic design optimization.

I. Introduction

NASA and Industry, recently ended the High Speed Civil Transport, HSCT, program. The objective of the HSCT program was to develop critical technologies to support the potential development of viable supersonic commercial transport aircraft. The initial phases of the HSCT program utilized the extensive database of methods and knowledge and expertise from the US Supersonic Transport, SST, program and the subsequent NASA sponsored Supersonic Cruise Research, SCR, studies. The aerodynamic design development activities benefited greatly from the use of the prior design, analysis and prediction methods as well as the understanding of the fundamental physics inherent in an efficient supersonic aircraft design. The emerging advanced Computational Fluid Dynamic methods greatly enhanced the supersonic design and analysis process and enabled substantial improvements in achievable aerodynamic performance levels. It was recognized that the critical strengths of the aerodynamic processes included the blending of the computational power offered by CFD methods with the fundamental knowledge and rapid design development and assessment capabilities inherent in the existing linear aerodynamic theory methods.

¹ Engineer/Scientist – Technical Fellow, Enabling Technology & Research, PO Box 3707, Seattle, WA 98124 / MS 67-LF, AIAA Member.

The primary objectives of this report are two fold. First, the Far-Field Composite Element supersonic wave drag optimization method, FCE, will be developed and introduced. Secondly the use of the universal parametric geometry representation method, CST^{1,2,3}, for wing design optimization will be demonstrated.

II. Planar Linear Theory Analyses vs CFD Analyses

One of the great joys of my career was to meet and become friends with Dr. Robert T. Jones. He possessed, among many other things, the remarkable ability to share his wisdom, blended with a touch of humor.

One time when discussing linear theory and CFD, he said with a twinkle in his eyes: *“Linear theory is long on ideas but short on arithmetic, CFD is long on arithmetic but short on ideas.”*

Although, linear theory can provide some unique insights and ideas, it does require understanding of both the numerical and physical limitations of the theory.

However CFD can provide both answers and visibility for flow solutions and flow conditions far beyond the capability of linear theory.

By using both CFD and linear theory and exploiting the benefits of each, we can have the “ideas” and the “arithmetic” plus the added bonus of increased synergistic understanding and design capability.

Since the advent of the utilization of the powerful CFD design and analysis methods, the value of linear theory methods is often questioned.

During the development cycle of a new airplane concept, an important question to be answered is “how much detail and computational sophistication is required? The answer offered to this question in reference 4 is *“In the spirit of Prandtl, Taylor and von Karman, the conscientious engineer will strive to use as conceptually simple as approach as possible to achieve his ends”*

Being “old” or restrictive does not imply “useless”. In fact many of the contributions derived from linear theory are still useful today:

- Elliptic load distribution for minimum induced drag
- Thin airfoil theory
- Conformal transformations
- Supersonic area rule wave drag calculation
- Transfer rule wing body optimization
- Sears-Haack, Haack-Adams and Karmen ogive minimum wave drag bodies of revolution
- Conical flow theory
- Reverse flow theorems
- Supersonic nacelle / airframe integration guidelines
- Supersonic favorable interference predictions and concepts
- Sonic boom prediction
- Understanding sonic boom configuration design factors
- Supersonic trade and sensitivity studies
- Baseline configuration for non-linear design optimization

Let us examine the fundamental differences in the results of linear theory analysis tools and results of corresponding non-linear CFD analysis.

Linear theory under estimates compression pressures and over estimates expansion pressures. In addition, linear theory disturbances are propagated along free stream Mach lines and therefore may not adequately predict shock formations. Linear theory with planar boundary conditions does not predict interferences between lift and volume. These differences typically are not significant effects for long slender, thin configurations at low lift coefficients, which correspond to the geometric characteristics of low drag supersonic configurations.

Linear theory equations as well as related direct solution formulations can provide direct insights and understanding into the effects of geometry on the nature of the flow phenomena. Because of the general ease of application and consistency of results, linear theory is often used for both sensitivity and trade studies. Linear theory can also be used to generate the large amount of data required for performance studies.

Linear theory as discussed in this report is linear potential flow theory with planar boundary conditions. Consequently it is easy to incorrectly apply the theory by application to configurations for which planar boundary conditions are not appropriate or in situations in which viscous effects become significant. It is therefore important to understand the limitations of linear theory and to use discretion when applying the theory so that the solutions are

physically meaningful. Properly used linear theory can predict the drag characteristics of well behaved configurations quite accurately.

Perhaps one of the most powerful attributes of linear theory is the superposition of fundamental solutions. This allows the separation of volume effects and lifting on aerodynamic forces. This property also allows superimposing influences of component parts of an aircraft to obtain the total forces on the aircraft. Superposition is the fundamental ingredient of the methodology presented in this report.

Early US SST development studies such as shown in figure 1, have confirmed that linear theory aerodynamic designs that satisfy the set of pressure coefficient limiting real flow design criteria described in references 5 and 6, achieve in the wind tunnel, the theoretical inviscid drag levels.

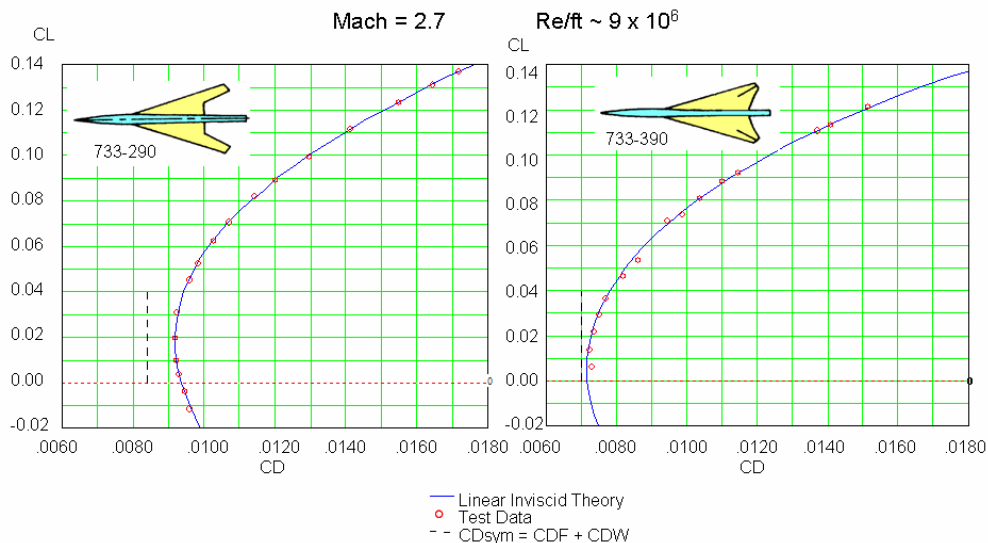


Figure 1. Early SST Linear Theory Optimized Configurations Test vs Theory Comparisons

The figure on the left is a comparison of the drag polar predicted by linear theory with Boeing test data for US SST model 733-290. This was a linear theory optimized design of the configuration that allowed Boeing to win the SST design development Government contract.

The friction drag, CDF, was computed by the T* method⁷. The volume wave drag, CDW, was calculated by Boeing developed zero lift wave drag program which was the basis for the NASA wave drag program⁸. The drag due to lift, CDL was calculated using the Boeing / NASA system of supersonic and analysis programs⁹. The linear theory prediction agrees very well with the test data.

The figure on the right is a comparison the linear theory predictions with test data for the US SST model 733-390. This was a linear design of the last variable sweep configuration that Boeing studied before the final switch to the US SST double delta configuration, B2707-300.

The same drag prediction methods were used as for the 733-290 configuration. Again, the linear theory prediction agrees very well with the test data

The designs developed by linear theory designs were heavily constrained by the real flow constraints^{5, 6} and are therefore considered to be on the conservative side in terms of the aerodynamic performance. Hence it is not surprising that the inviscid predictions of drag match the wind tunnel test data

Force calculations obtained with the inviscid and viscous CFD and with linear theory, are compared with wind tunnel test data at Mach 2.4 in figure 2 for two refined linear theory designs developed during HSCT program.

The inviscid codes included linear theory, the TRANAIR full potential code, and a parabolized Euler code. The viscous analyses were obtained with a parabolized Navier-Stokes code. Flat plate skin friction drag estimates were added to the inviscid CFD drag calculations, and to the linear theory and Euler predictions to obtain the total aerodynamic drag. The viscous and inviscid lift and drag predictions all agree quite well with the test data. The linear theory drag predictions depart from the test data at the higher CL above the design condition.

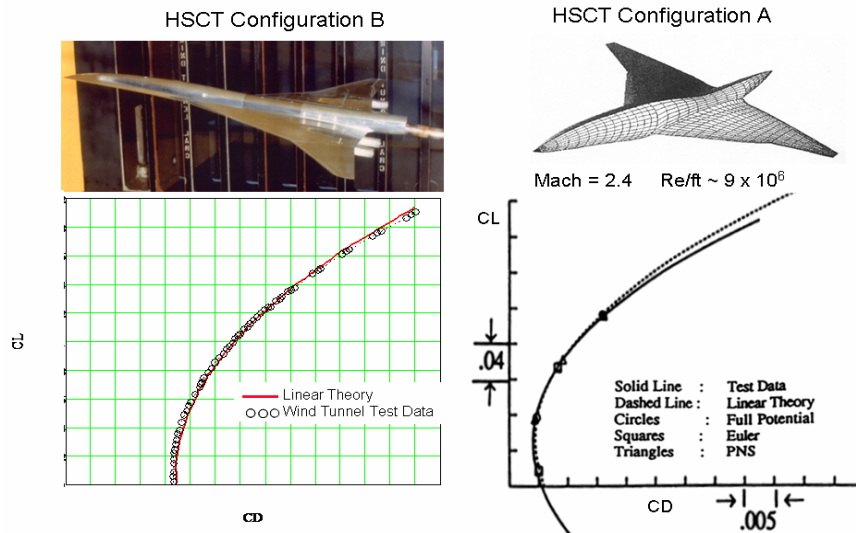


Figure 2. Typical HSCT Configurations Drag Polars Mach = 2.4

These various test versus theory comparisons illustrate that linear theory as used in this report can provide accurate assessments of the aerodynamic forces near the 1 g cruise conditions which typically correspond to the design optimization conditions. These results together with extensive experience on the HSCT program indicate that a good initial linear theory optimized design can provide basis for developing non-linear CFD optimized designs.

III. Supersonic Drag Components

The drag components of a slender supersonic configuration flying at supersonic speeds consists primarily of friction drag, wave drag due to volume, wave drag due to lift, induced drag and other miscellaneous drag items as shown if Figure 3.

- $CD = CD_F + CD_{WV} + CD_{WL} + CDI + CD_{MISC}$

- $CD_F \approx \text{WETTED AREA} \Rightarrow \text{FRICTION DRAG}$

- $CD_{WV} \approx Vol^2 / L_s^4 \Rightarrow \text{VOLUME WAVE DRAG}$

- $CD_{WL} \approx (LIFT/X_s)^2 \Rightarrow \text{LIFT WAVE DRAG}$

- $CDI \approx (LIFT/b)^2 \Rightarrow \text{INDUCED DRAG}$

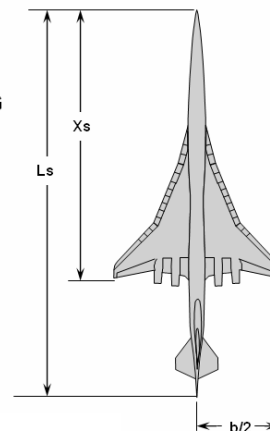


Figure 3 Supersonic Drag Components

The friction drag is typically equal to flat plate skin friction drag on all of the component surfaces. The friction drag, therefore, depends primarily on the wetted area.

The volume wave drag of a slender supersonic type configuration, to a first order, varies with the overall volume of the configuration squared divided by the configuration length raised to the fourth power. The induced drag varies

with the ratio of lift over wing span squared. The wave drag due to lift varies with lift over the streamwise length of the lifting surface squared. The wave drag due to lift vanishes as the supersonic Mach number approaches one.

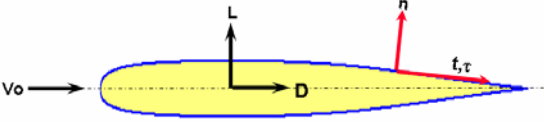
It is evident that for low drag, supersonic configurations tend to be long, thin and slender. The higher the cruise speed, the more slender is the lowest drag configuration.

The most common way to calculate drag is to sum the forces acting normal to the surface plus the forces acting tangential to the surface as shown in figure 4.

The net drag force acting normal to the surface is known as *pressure drag*. The forces acting tangential to the surface results from the action of viscosity and is called *viscous drag or skin friction*.

The pressure drag is equal to the integral of the surface pressure times the cosine of the angle between the surface local outward normal and the free stream velocity direction. The viscous drag is equal to the integral of the local shear stress times the cosine of the angle between the local surface slope and the free stream velocity direction.

The process of calculating forces by integration of the surface pressures and shear stress over the surface is commonly called *Near Field Theory*. This is the process typically used in non-linear CFD codes.



Pressure Drag:
$$D_p = - \iint_S p \cos(n, V_o) dS$$

- Volume Wave Drag
- Wave Drag Due to Lift Plus Induced Drag
- Base Pressure Drag

Viscous Drag:
$$D_v = \iint_S \tau \cos(t, V_o) dS$$

Figure 4 Near Field Calculation Approach

With linear theory, the use the near field theory approach has a number of both positive and negative features, as well as a number of negative features¹⁰ as indicated in figure 5.

The near field approach has been used to develop the conventional methods for linear theory wing camber / twist optimization. The distributions of basic lift, drag and interference forces can be determined. The nature of the flow can be judged from the surface pressure distributions. It is possible to include real flow limiting criteria in the design processes. Semi-empirical corrections can be included to provide useful hybrid design and analysis methods. It is also possible to incorporate higher order corrections to the basic theory.

The near field methods most often require sophisticated numerical methods to evaluate the solution integrals. Often special care is necessary to properly account for the leading edge forces. Although these are normally transparent to the user, they can affect the numerical accuracy of the solution.

Unless the physical and mathematical limitations are known, it is also easy to misuse the theory and the methods. Because of the linearized boundary conditions, the analysis configurations must be planar. It is possible and often necessary to properly account for interference effects for non-planar component arrangements such as wing / nacelle interactions with slight modifications to the theory.

- “+” Direct Approach for Wing Camber / Twist Optimization
- “+” Can Provide Distributions of Basic Drag and Interference Forces
- “+” Can Judge Analyses or Designs From Cp's
- “+” Can Include Real Flow Criteria or Limitations
- “+” Can Include Semi-empirical Corrections to the Methods
- “+” Can Include Higher Order Corrections to the Theory
- “-” Usually Requires Sophisticated Numerical Methods
- “-” Care Required to Deal With Edge Forces (e.g. Leading Edge Suction) and Shapes (e.g. Round Leading edge)
- “-” Easy to Misuse the Theory and Methods – by Not Understanding Limitations or Not Understanding the Implied Boundary Layer Conditions
- “-” Usually Requires Simulation of Configuration Symmetry
- “-” May Miss Significant Interference Interactions

Figure 5: Near Field Linear Theory Positive and Negative Features
American Institute of Aeronautics and Astronautics

An alternate way to calculate the drag of a configuration is to use a “*Far-Field Theory*” approach as shown in figure 6.

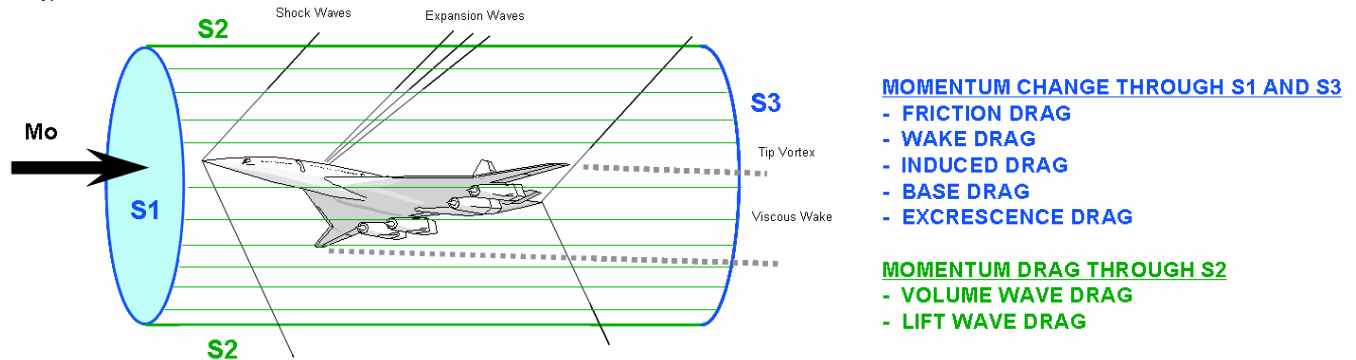


Figure 6 Far Field Drag Calculation Approach

In this approach, the drag of the configuration is determined from streamwise momentum change, through a control volume containing the configuration.

The control volume typically is cylindrical. The upstream end, S1 has only free stream undisturbed flow passing through it. The downstream surface, S3, is located far enough down stream of the configuration that the pressure induced flow field becomes essentially two dimensional. This is often called the Trefftz plane. The momentum change between side S1 and Side S3 is due primarily to the friction drag and the induced drag. Miscellaneous drag items such as wake drag, base drag and excrescence drag are also related to the momentum changes between S1 and S3.

The cylindrical sides are many body lengths away. At subsonic Mach numbers the flow becomes parallel to the sides of the cylinder and hence there is no flow through this surface and hence no momentum change. At supersonic speeds, because of the shock waves and the expansion waves generated by the configuration, there is mass flow in and out of the cylinder through the sides. The streamwise momentum associated with this mass flow across the sides of the cylinder is called the wave drag. Since the shock wave structure around a supersonic configuration can change with angle of attack, the wave drag can also vary with angle of attack. Hence the wave drag consists of the wave drag due to the volume distribution of the configuration plus the variation of wave drag with lift which is called “wave drag due to lift”.

The Far Field Linear Theory has a number of both positive and negative features ¹⁰ as shown in figure 7.

- “+” **Easy Numerical Formulations**
- “+” **No Problem With Linear Theory Leading Edge Forces**
- “+” **Easy Volume Wave Drag Calculation**
- “+” **Can separate Induced Drag and Wave Drag Due to Lift**
- “+” **Direct Approach for Wing / Body Area Rule Optimization**
- “+” **New Wing Thickness / Airfoil Optimization Method**
- “+” **New Induced Drag + Wave Drag Due to Lift Optimization Method**
- “+” **Useful for Lower Bound Supersonic Drag Assessments**

- “-” **Can’t Directly Judge Analyses or Designs**
- “-” **Very Easy to Misuse the Theory and Methods**
- “-” **Requires Simulation of Configuration Symmetry**
- “-” **Requires Special Treatment of Non- Planar Arrangements Such as Wing / Nacelles**
- “-” **Can not Easily incorporate Semi-Empirical theory corrections to predictions or analyses**

American Institute of Aeronautics and Astronautics

Figure 7: Far-Field Linear Theory Positive and Negative Features

On the positive side, the mathematical formulations of Far-Field Theory, are rather easy and have no difficulty in dealing with linear theory leading edge forces. The far-field codes provide an easy and consistent approach to evaluate the volume wave drag of a configuration. The far field wave drag method provides a simple and direct method for body area rule design optimization. Calculation of either induced drag or wave drag to lift by a far field method, requires that the lift distribution be known. Consequently, this method is not normally used to compute drag due to lift since the near-field method would have to be used initially to obtain the lift distribution. Hence the drag due to lift would already be available from the near field analysis..

On the negative side, The far-field optimum designs can not be directly judged to assess the potential for success of a particular design. As is the case with any linear theory, it is easy to misuse the theory and the methods. The far field wave drag method essentially requires that the configuration be planar and symmetric. However, it is possible to use images to allow the meaningful analysis of non-planar arrangements such as wing / nacelles. More extensive discussions of supersonic wave drag are contained in reference 10.

IV. Far-Field Supersonic Wave Drag Calculation

As previously mentioned the wave drag of a supersonic configuration is equal to the change in streamwise momentum due to the mass flow into and out of the side of the control volume. Heaslet and Lomax^{11, 12, 13} and R.T. Jones¹⁴ showed that the momentum loss through the cylindrical sides of the control volume could be calculated as the wave drag of a series of equivalent volume bodies. The streamwise area distributions of the equivalent bodies are determined by normal projections of the total local area of the configuration cut by oblique cutting planes through the analysis configuration at each stream wise station. The cutting planes are tangent to the freestream Mach cones as shown in figure 8.

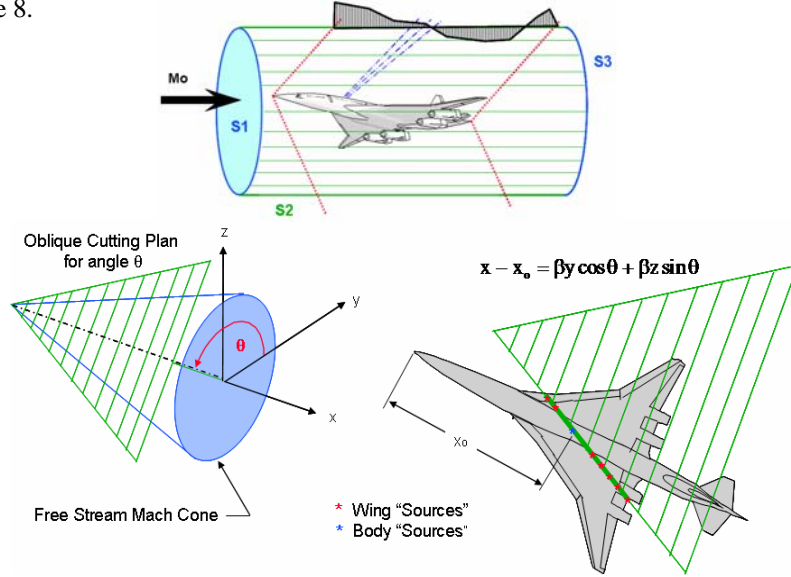


Figure 8 Far Field Wave Drag Calculation

The cutting planes are identified by the tangency angle θ as shown in the figure. The $\theta = 90^\circ$ cutting plane is tangent to the top of the Mach forecone. This defines the moment loss through the thin streamwise strip on top of the control volume. The $\theta = 0^\circ$ cutting plane is tangent to the side of the Mach cone and defines the loss of momentum through the thin strip on the side of the control volume. The cutting planes identified by values of θ between 0° and 90° define the momentum loss in the streamwise strips around the cylinder between the top and the side. For a symmetric configuration, the momentum loss is symmetric in all quadrants. The total wave drag of the configuration is equal to the integrated sum of the momentum losses around the surface of the control volume as shown in equation 1.

$$\frac{D_w}{q} = -\frac{1}{4\pi^2} \int_0^{2\pi} d\theta \int_0^{l(\theta)} \int_0^{l(\theta)} A''(x, \theta) A''(\xi, \theta) \ln|x - \xi| dx d\theta \quad (1)$$

The equation that defines the various cutting planes is $x - \beta y \cos \theta - \beta z \sin \theta = x_0$ (2)

Where $\beta = \sqrt{M^2 - 1}$ and $A(x, \theta)$ is the equivalent body area distribution determined for the cutting plane “ θ ”.

It is well known that the Sears-Haack body is the minimum wave drag body of revolution for a given volume at supersonic speeds¹⁰. Consequently the lowest wave drag for any planar type configuration would occur if every $A(\theta, x)$ area distribution in equation 1 had an area distribution corresponding to that of a Sears-Haack body. This is not a feasible situation for any wing planform other than a yawed elliptic wing. How this normally fictitious drag level does define the absolute lower bound wave drag for a given configuration.

The wave drag of a configuration can be easily calculated using the supersonic area rule theory programs described in references 6 and 7.

Figure 9 shows results of wave drag calculations for a supersonic wing plus body configuration at Mach 2.4. The wave drag distribution around the configuration is shown along with the Mach 1 drag distribution. The maximum drag occurs for $\theta = \pm 90$ degrees which is above and below the configuration. The drag at these stations is equal to that at Mach 1. Some of the combined area distribution plots are shown for different angular stations around the configuration. At the higher Mach number, the angular distribution rapidly decreases to a minimum off to the side of the configuration. This is associated with the peak of the wing area distribution being reduced and the wing volume spread over a longer length.

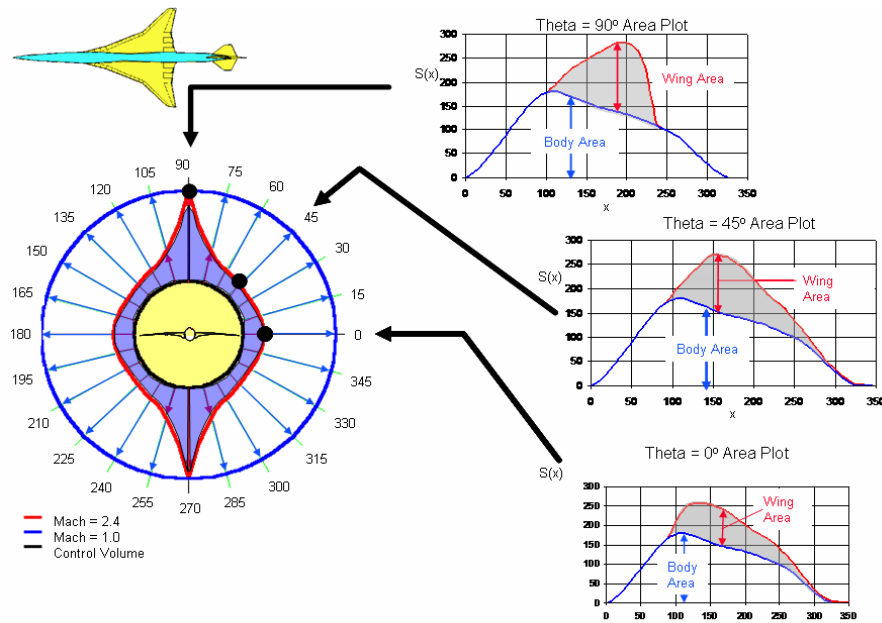


Figure 9: Wave Drag Distribution Around a Typical Supersonic Transport

V. CST Method Analytic Representation of a Wing for Design Optimization

For aerodynamic design optimization, it is very desirable to limit the number of the geometric design variables. In reference 1, a “fundamental” parametric airfoil geometry representation method, was presented. The method included the introduction of a geometric “Class function / Shape function” Transformation technique, “CST”, such that round nose / sharp aft end geometries as well as other classes of geometries can be represented exactly by analytic well behaved and simple mathematical functions having easily observed physical features. The fundamental parametric geometry representation method was shown to describe an essentially limitless design space composed entirely of analytically smooth geometries. The “class function / shape function” methodology was extended^{2,3} to more general three dimensional applications such as wing, body, ducts and nacelles. It was shown that a general 3D geometry can be represented by a distribution of fundamental shapes, and that the “class function / shape function” methodology can be used to describe the fundamental shapes as well as the distributions of the fundamental shapes. With this very robust, versatile and simple method, a 3D geometry is defined in a design space by the distribution of class functions and the shape functions. This design space geometry is then transformed into the physical space in which the actual geometry is defined.

The concept of “analytic scalar definitions using composite wing surfaces” was also presented. The composite wing shapes can be used for design optimization and parametric design studies.

One of the objectives of the studies presented in this report was to evaluate the usefulness of the scalar wing concept for design optimization. A brief description and review of the CST methodology will be shown since knowledge of this information is essential to the understanding of the utilization of the methodology that is presented in the present paper.

The CST method was originally developed to provide a mathematically efficient representation of an airfoil. For a round nose airfoil described in a fixed Cartesian coordinate system, the slopes and 2nd derivatives of the surface geometry are infinite at the nose and large changes in curvature occur over the entire airfoil surface. The mathematical characteristics of the airfoil surfaces are therefore non-analytic function with singularities in all derivatives at the nose. The mathematical description of an airfoil must therefore deal with a rather complex non-analytic function over the surface of the airfoil. Consequently a large number of “x,z” coordinates are typically required along with a careful choice of interpolation techniques in order to provide a mathematical or numerical description of the surfaces of a cambered airfoil.

In reference 1, it was shown that the surface coordinates for any airfoil with zero trailing edge thickness can be mathematically defined as the product of two functions:

$$\zeta(\psi) = C_{N2}^{N1}(\psi) \bullet S(\psi) \quad (3)$$

Where: $\psi = x/c$ and $\zeta = z/c$

The term $C_{N2}^{N1}(\psi)$ is called the class function and is defined by the equation:

$$C_{N2}^{N1}(\psi) = \psi^{N1} \bullet [1 - \psi]^{N1} \quad (4)$$

The class function for an round nose airfoil with a sharp trailing edge as shown in figure 10, has the class function exponents $N1 = 0.5$ and $N2 = 1.0$. An airfoil with a sharp nose airfoil has the class function exponent $N1 = N2 = 1.0$.

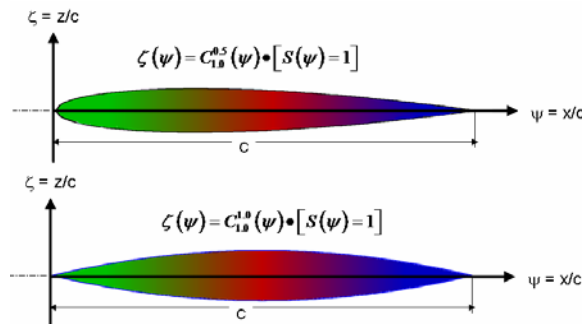


Figure 10: Unit Shape Function Round Nose and Sharp Nose Airfoils

The term $S(\psi)$ is called the shape function and can be easily determined from any specified airfoil geometry by the equation

$$S(\psi) \equiv \frac{\zeta(\psi)}{C_{N2}^{N1}(\psi)} \quad (5)$$

The “shape function” equation that describes an airfoil is a simple well behaved analytic equation that can be easily represented by a relatively small number of parameters. The shape function also has the unique feature that the nose radius, and the boat-tail angle are directly related to the bounding values of the “ $S(\psi)$ ” function.

The value of the shape function at $x/c = 0$ is directly related to the airfoil leading edge nose radius by the relation:

$$S(0) = \sqrt{2R_{LE}/C} \quad (6)$$

The value of the shape function at $x/c = 1$ is directly related to the airfoil boat-tail angle, β , by the relation:

$$S(1) = \tan \beta + \frac{\Delta Z_{te}}{C} \quad (7)$$

An example of the transformation of an airfoil geometry to the corresponding shape function is shown in figure 11. The transformation of the constant Z_{max} height line, and the constant boat-tail angle line, are also shown in the figure.

The shape function for this example airfoil is seen to be approximately a straight line with the value at zero related to the leading edge radius of curvature and the value at the aft end equal to tangent of the boat-tail angle plus the ratio of trailing edge thickness / chord length. It is readily apparent that the shape function is indeed a very simple analytic function.

The areas of the airfoil that affects its drag and performance characteristics of the airfoil are readily visible on the shape function curve as shown in the figure. Furthermore, the shape function provides easy control of the airfoil critical design parameters.

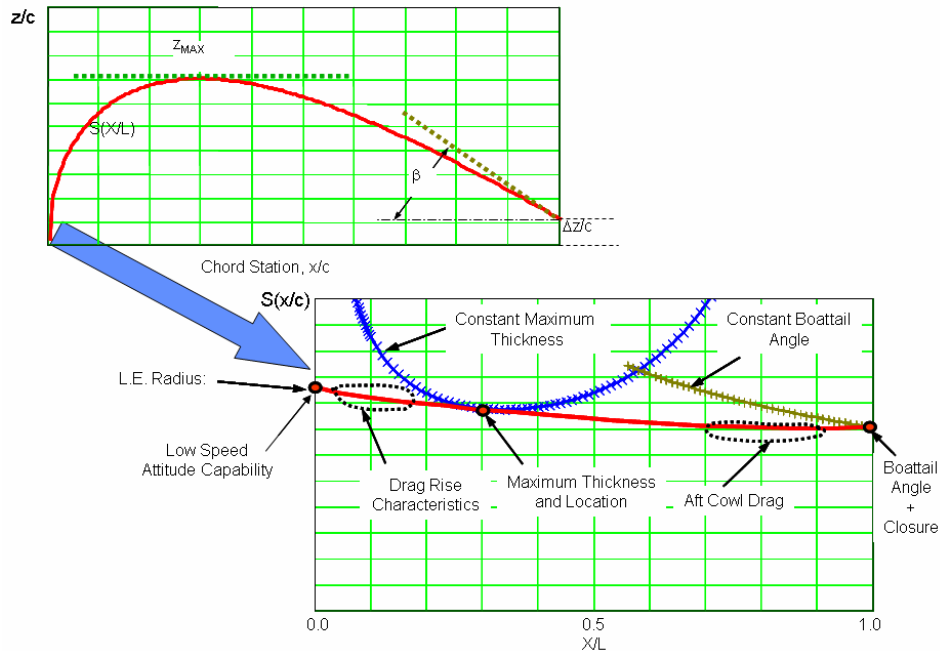


Figure 11: Example of an Airfoil Geometric Transformation

The simplest of all shape functions the constant unit shape function and is defined as $S(\psi) = 1$. The unit shape function in combination with various sets of class function define a wide variety of basic geometric shapes.

$\zeta(\psi) = C_{1.0}^{0.5}(\psi) \rightarrow$ Defines a NACA type round nose and pointed aft end airfoil.

$\zeta(\psi) = C_{0.5}^{0.5}(\psi) \rightarrow$ Defines an elliptic airfoil, or body of revolution

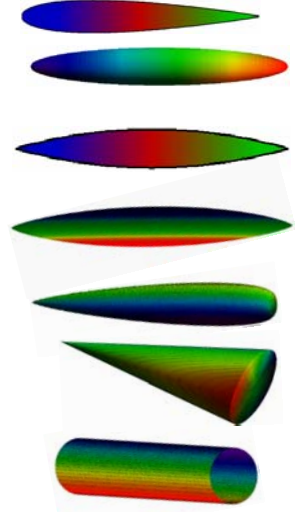
$\zeta(\psi) = C_{1.0}^{1.0}(\psi) \rightarrow$ Defines a biconvex airfoil, or an ogive body.

$\zeta(\zeta) = C_{0.75}^{0.75}(\psi) \rightarrow$ Defines the radius distribution of a Sears-Haack body

$\zeta(\psi) = C_{0.25}^{0.75}(\psi) \rightarrow$ Defines a low drag projectile

$\zeta(\psi) = C_{0.001}^{1.0}(\psi) \rightarrow$ Defines a cone or wedge airfoil.

$\zeta(\psi) = C_{0.001}^{0.001}(\psi) \rightarrow$ Defines a rectangle, or circular rod.



The “class function” defines the general classes of geometries, where as the “shape function” is used to define specific shapes within the geometry class.

The unit shape function can be decomposed into scalable component airfoils¹ by representing the shape function with a Bernstein polynomial of order “N” .

The representation of the unit shape function in terms of increasing orders of the Bernstein polynomials provides a systematic decomposition of the unit shape function into scaleable components. This is the direct result of the “Partition of Unity” property which states that the sum of the terms, which make up a Bernstein polynomial of any order, over the interval of 0 to 1, is equal to one. This means that every Bernstein polynomial represents the unit shape function. Consequently, the individual terms in the polynomial can be scaled to define an extensive variety of airfoil geometries¹.

The Bernstein polynomial of any order “n” is composed of the “n+1” terms of the form:

$$S_{r,n}(x) = K_{r,n} x^r (1-x)^{n-r} \quad (8)$$

r = 0 to n

n = order of the Bernstein polynomial

In the above equation, the coefficients factors $K_{r,n}$ are binominal coefficients defined as:

$$K_{r,n} \equiv \binom{n}{r} \equiv \frac{n!}{r!(n-r)!} \quad (9)$$

For any order of Bernstein polynomial selected to represent the unit shape function, only the first term defines the leading edge radius and only the last term defines the boat-tail angle. The other in-between terms are “shaping terms” that neither affect the leading edge radius nor the trailing edge boat-tail angle.

Examples of decompositions of the unit shape function using various orders of Bernstein polynomials are shown in figure 12 along with the corresponding composite airfoils that are obtained by multiplying the component shape function by the class function.

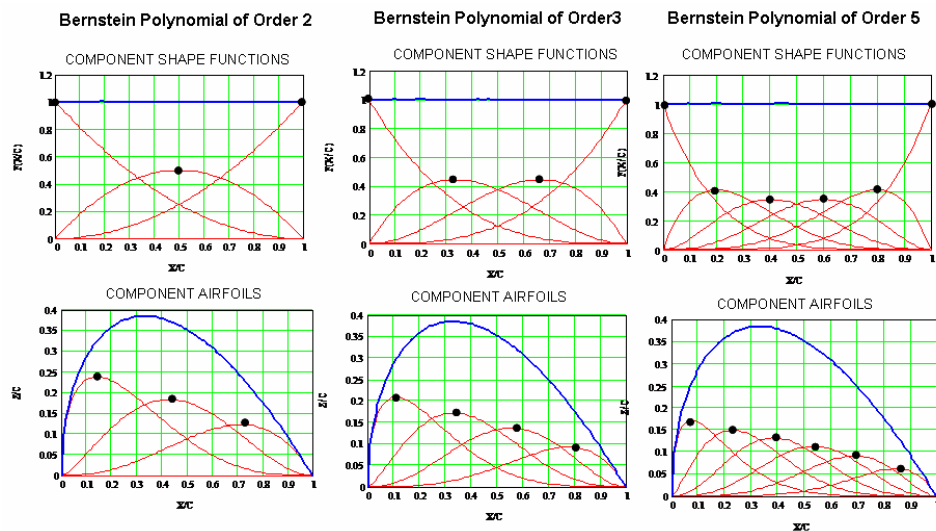


Figure 12: Bernstein Polynomials Provides “Natural Shapes”

The technique of using Bernstein polynomials to represent the shape function of an airfoil in reality defines a systematic set of component airfoil shapes that can be scaled to represent a variety of airfoil geometries as illustrated in figure 13

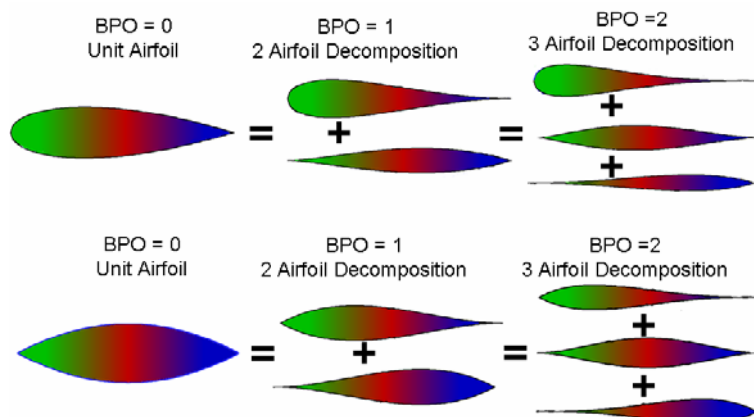


Figure 13: Example Component Airfoils

The method of utilizing Bernstein polynomials to represent an airfoil has the following unique and very powerful properties¹:

- This airfoil representation technique, captures the entire design space of smooth airfoils
- Every airfoil in the entire design space can be derived from the unit shape function airfoil
- Every airfoil in the design space is therefore derivable from every other airfoil

Using Bernstein polynomials, the general equation for the shape function of any symmetric airfoil can be

$$\text{expressed as: } S(\psi) = \sum_{i=0}^{N_x} Ax_i \bullet S_i(\psi) \quad (10)$$

where N_x is the order of the selected Bernstein polynomial.

The equation defining the airfoil coordinates is;

$$\zeta(\psi) = C_{N_2}^{N_1}(\psi) \bullet S(\psi) = \sum_{i=0}^{N_x} Ax_i \bullet C_{N_2}^{N_1}(\psi) \bullet S_i(\psi) \quad (11)$$

The coefficients Ax_i can be determined by a variety of techniques depending on the objective of the particular study. Some examples include:

- Variables in a numerical design optimization application
- Least squares fit to match a specified geometry
- Parametric shape variations.

A 3D wing can be considered to be a distribution of airfoils across the wing span. Sectional applications of the shape function can thus produce an analytic shape function surface describing the entire wing. It was shown in reference 2 that the shape function surface for a complete wing surface can be obtained by first representing the root airfoil shape function by a Bernstein polynomial of a specified order. The complete wing shape function surface can then be defined by expanding the coefficients of the chordwise Bernstein polynomial, in the spanwise direction using any appropriate numerical technique. The surface definition of the wing is then obtained by multiplying the shape function surface by the wing class function. This in essence provides an analytic scalar definition of any wing surface.

In this report we will use the Bernstein polynomial formulation to represent both the streamwise airfoil shapes by a set of composite airfoils, as well as for describing the spanwise variation of the magnitude of each composite airfoil across the wing span.

The mathematical description of the wing surface is easily obtained by expanding the airfoil “ Ax_i ” coefficients in the spanwise direction using Bernstein polynomials of order “ N_y ” as:

$$Ax_i(\eta) = \sum_{j=0}^{N_y} B_{i,j} Sy_j(\eta) \quad (12)$$

$$\text{Where } Sy_j(\psi) = Ky_j \eta^j (1-\eta)^{N_y-j} \quad \text{for } j = 0 \text{ to } N_y \quad (13)$$

$$\text{And } Ky_j \equiv \binom{N_y}{j} \equiv \frac{N_y!}{j!(N_y-j)!} \quad (14)$$

The symmetric wing surface is then defined by:

$$\zeta(\psi, \eta) = \sum_i^{N_x} \sum_j^{N_y} \left[B_{i,j} Sy_j(\eta) \{ C_{N_2}^{N_1}(\psi) Sx_i(\psi) \} \right] \quad (15)$$

The coefficients $B_{i,j}$ will be the design optimization for the studies described in this report.

This process of defining a wing geometry, may be considered a **scalar loft** of a wing where every points on the wing surface is defined as accurately as desired and the points are all “connected” by the analytic equations. This is in contrast to the usual wing definition of a **vector loft** of a wing which is defined as ordered sets of x,y,z coordinates plus “rules” that describe how to connect adjoining points. The common approach used in most vector lofts is to connect adjacent points is along constant span stations and along constant percent chord lines.

In equation 15, each term $\zeta_{ij}(\psi, \eta) = C_{N2}^{N1}(\psi) Sx_i(\psi) Sy_j(\eta)$ defines a composite wing geometry formed by the “ith” component airfoil shape $C_{N2}^{N1}(\psi) Sx_i(\psi)$ with the ‘jth’ spanwise variation $Sy_j(\eta)$.

The total wing is then represented by a total of “Nt” scalable composite wing elements, where

$$Nt = (Nx + 1) \cdot (Ny + 1) \quad (16)$$

VI. “FCE” Wing Representation as Composite Elements

The finite composite element, “FCE” optimization method will be formulated using the previously discussed CST analytic wing representation method.

The Wing will be represent as a set of Composite Wing Elements. First select the order of the Bernstein polynomial, Nx, to define the set of composite airfoil shapes. Then select the order of the Bernstein polynomial, Ny, to define the spanwise variations of the composite airfoil shapes. The total number of resulting composite wing shapes is given by equation 16. The Total Wing surface is then defined by :

$$\zeta(\psi, \eta) = \sum_{j=0}^{Ny} Sy_j(\eta) \sum_{i=0}^{Nx} B_{i,j} \left[C_{1.0}^{0.5}(\psi) Sx_i(\psi) \right] \quad (17)$$

It is convenient to convert this matrix representation of the wing shape into an equivalent vector definition. This can be achieved using the following transformation process.

An “i,j” matrix can be converted into a “k” element vector using transformation.

$$\text{Define } zz_{k,0} \triangleq \text{trunc} \left(\frac{k}{Ny+1} \right) \quad \text{and} \quad zz_{k,1} \triangleq k - (Ny+1) \cdot \text{trunc} \left(\frac{k}{Ny+1} \right) \quad (18)$$

Where $k = 0$ to $Nt-1$

$$\text{Let } ik_k = zz_{k,0} \quad \text{and} \quad jk_k = zz_{k,1}$$

$$\text{By substitution: } \zeta(\psi, \eta)_k \equiv \zeta(\psi, \eta)_{ik_k, jk_k} \quad (19)$$

Each of the k Composite wings has a corresponding wing volume V_k , that is obtained by integration of the corresponding composite wing thickness distribution over the wing planform area. This integrated volumes are obtained as part of the wave drag analysis of each composite wing.

$$\text{The total base wing volume is given by: } V_{Base} = \sum_{k=1}^{Nt} V_k$$

As previously shown in equation 1, the wave drag of an isolated wing can be calculated from the area distribution of the wing as:

$$\frac{D}{q} = -\frac{1}{4\pi^2} \int_0^{2\pi} d\theta \int_0^{l(\theta)} \int_0^{l(\theta)} A''(x, \theta) A''(\xi, \theta) \ln|x - \xi| dx d\theta$$

The total wing area can be represented as the sum of the areas of the fundamental wing elements as:

$$A(x, \theta) = \sum_{i=1}^{Nt} A_i(x, \theta) \quad (20)$$

$$\text{By substitution: } CD_w = \frac{1}{2\pi S_{Ref}} \int_0^{2\pi} \int_0^{l(\theta)} \int_0^{l(\theta)} \sum_{i=1}^{Nt} A_i''(x, \theta) \sum_{j=1}^{Nt} A_j''(x, \xi) \ln|x - \xi| dx d\xi d\theta \quad (21)$$

Interchanging the order of integration and summation yields:

$$CD_w = \frac{1}{2\pi S_{Ref}} \sum_{i=1}^{N_t} \sum_{j=1}^{N_t} \int_0^{2\pi l(\theta)} \int_0^{l(\theta)} A_i''(x, \theta) A_j''(x, \xi) \ln|x - \xi| dx d\xi d\theta \quad (22)$$

The total wave drag can then be written as the double sum:
$$CD_w = \sum_{i=1}^{N_t} \sum_{j=1}^{N_t} CD_{ij} \quad (23)$$

Where:
$$CD_{ij} \triangleq \frac{1}{2\pi S_{Ref}} \int_0^{2\pi l(\theta)} \int_0^{l(\theta)} A_i''(x, \theta) A_j''(x, \xi) \ln|x - \xi| dx d\xi d\theta \quad (24)$$

For $i = j$: CD_{ii} is the drag of fundamental element “AiAi”.

For $i \neq j$: $CD_{ij} + CD_{ji}$ is the interference drag between element “Ai and element “Aj”.”

For simplicity we will use the notation:
$$CD_{ij}^{\hat{}} \triangleq CD_{ij} + CD_{ji} \quad \text{for } i \neq j \quad (25)$$

and
$$CD_{ii}^{\hat{}} \triangleq CD_{ii} \quad \text{for } i = j \quad (26)$$

Therefore the total wave drag is equal to the sum of the wave drag of each isolated volume component plus the mutual interference drag between each pair of volume elements.

The isolated drag of any of the fundamental elements can be obtained by computing⁷ the wave drag in which the “wing” analysis geometry is represented by the single component wing geometry

In order to calculate the mutual interference drag between any of the two wing elements we will use the identity:

$$(A_i + A_j)^2 \equiv (A_i)^2 + 2A_i A_j + (A_j)^2 \quad (27)$$

And therefore:
$$2A_i A_j \equiv (A_i + A_j)^2 - (A_i)^2 - (A_j)^2$$

Consequently
$$CD_{ij}^{\hat{}} = CD(A_i + A_j) - CD(A_i) - CD(A_j) \quad (28)$$

The interference drag between any of two wing elements i and j can therefore, be determined by calculating the drag of a wing composed of the sum of the two wing components i and j and then subtracting the drags of the individual elements.

The total wing drag in terms of the drags of the fundamental elements is equal to:

$$CD_w = \sum_{i=1}^{N_t} \sum_{j \neq i,=1}^{N_t} CD_{ij}^{\hat{}} \quad (29)$$

The total number of individual required composite wing wave drag analyses, N_{Cal} , equals:

$$N_{Cal} = \frac{N^2 + N}{2} \quad (30)$$

An example of the far field wave drag component matrix for a six composite element wing is shown in figure 14

	A ₁	A ₂	A ₃	A ₄	A ₅	A ₆
A ₁	\hat{CD}_{11}	$2\hat{CD}_{12}$	$2\hat{CD}_{13}$	$2\hat{CD}_{14}$	$2\hat{CD}_{15}$	$2\hat{CD}_{16}$
A ₂		\hat{CD}_{22}	$2\hat{CD}_{23}$	$2\hat{CD}_{24}$	$2\hat{CD}_{25}$	$2\hat{CD}_{26}$
A ₃			\hat{CD}_{33}	$2\hat{CD}_{34}$	$2\hat{CD}_{35}$	$2\hat{CD}_{36}$
A ₄				\hat{CD}_{44}	$2\hat{CD}_{45}$	$2\hat{CD}_{46}$
A ₅					\hat{CD}_{55}	$2\hat{CD}_{56}$
A ₆						\hat{CD}_{66}

Figure 14: Wave Drag Matrix for a Six Composite Element Wing

VII. Isolated Wing Optimization.

In order to formulate the wing optimization process we will introduce the “to be determined” composite wing thickness scaling factors S_i , so that the “ith” composite wing element thickness distribution and its corresponding elementary volume scale linearly with S_i .

The total scaled wing volume, Vol, is therefore:
$$Vol = V_{Base} V_R = \sum_{i=1}^{Nt} S_i V_i \quad (31)$$

V_{Base} is the original un-scaled wing volume and V_R is the ratio of the desired wing volume to the original wing volume.

The scaled wing half thickness distribution equation becomes:
$$\zeta(\psi, \eta) = \sum_{i=1}^{Nt} s_i \zeta_i(\psi, \eta) \quad (32)$$

The wing area distribution becomes:
$$A(x, \theta) = \sum_{i=1}^{Nt} s_i A_i(x, \theta) \quad (33)$$

Consequently, the scaled wing wave drag becomes:
$$CD_W = \sum_{i=1}^{Nt} \sum_{j=1}^{Nt} (s_i s_j \hat{CD}_{ij}) \quad (34)$$

It is convenient to write the volume equation in terms of the original wing volume fraction ratios v_i . This defines the fraction of the total wing volume that is due the composite wing element “i”

$$v_i \triangleq \frac{V_i}{V_{Base}} \quad (35)$$

The total volume equation becomes
$$V_R = \sum_{i=1}^{Nt} \frac{s_i V_i}{V_{Base}} = \sum_{i=1}^{Nt} s_i v_i \quad (36)$$

Let
$$\tilde{D}_{ij} \triangleq \frac{\hat{CD}_{ij}}{v_i v_j} \quad (37)$$

Introduce the condensed volume fraction scaling factor
$$k_i = s_i v_i \quad (38)$$

The wing volume equation becomes
$$V_R = \sum_{i=1}^{Nt} k_i \quad (39)$$

The wave drag equation is
$$CD_W = \sum_{i=1}^{Nt} \sum_{j=1}^{Nt} (k_i)(k_j) \tilde{D}_{ij} \quad (40)$$

We can now define our optimization problem as determining the unknown coefficients “ k_i ” to minimize the wave drag in equation 40 for a given volume ratio V_R defined by equation 39.

The volume equation can be written as a linear constraint equation as:

$$\Phi_V = 0 = V_R - \sum_{i=1}^N k_i \quad (41)$$

The optimization problem can be formulated using a Lagrange’s multiplier λ_V .

Define
$$F = CD_W - \lambda_V \Phi_V \quad (42)$$

The solution for minimum wave drag subject to the volume constraint equation 21, can then be determined from the system of linear equations derived from equation 22 as.

For $i = 1$ to N
$$\frac{\partial F}{\partial k_i} = 0 \quad \text{and} \quad \frac{\partial F}{\partial \lambda_V} = 0 \quad (43)$$

This provides the complete system of $N+1$ linear equations to determine the $N+1$ unknowns.

The system of linear equations to solve are:

$$\frac{\partial F}{\partial k_i} = 2\tilde{D}_{ii}k_i + \sum_{j=1, j \neq i}^{Nt, Nt} \tilde{D}_{ij}k_j + \lambda_V = 0 \quad (44)$$

And
$$\frac{\partial F}{\partial \lambda_V} = \sum_{i=1}^{Nt} k_i - V_R = 0 \quad (45)$$

For example, the set of equations for a six component wing optimization are:

$$\begin{aligned} 2\tilde{D}_{11}k_1 + \tilde{D}_{12}k_2 + \tilde{D}_{13}k_3 + \tilde{D}_{14}k_4 + \tilde{D}_{15}k_5 + \tilde{D}_{16}k_6 + \lambda_V &= 0 \\ \tilde{D}_{21}k_1 + 2\tilde{D}_{22}k_2 + \tilde{D}_{23}k_3 + \tilde{D}_{24}k_4 + \tilde{D}_{25}k_5 + \tilde{D}_{26}k_6 + \lambda_V &= 0 \\ \tilde{D}_{31}k_1 + \tilde{D}_{32}k_2 + 2\tilde{D}_{33}k_3 + \tilde{D}_{34}k_4 + \tilde{D}_{35}k_5 + \tilde{D}_{36}k_6 + \lambda_V &= 0 \\ \tilde{D}_{41}k_1 + \tilde{D}_{42}k_2 + \tilde{D}_{43}k_3 + 2\tilde{D}_{44}k_4 + \tilde{D}_{45}k_5 + \tilde{D}_{46}k_6 + \lambda_V &= 0 \\ \tilde{D}_{51}k_1 + \tilde{D}_{52}k_2 + \tilde{D}_{53}k_3 + \tilde{D}_{54}k_4 + 2\tilde{D}_{55}k_5 + \tilde{D}_{56}k_6 + \lambda_V &= 0 \\ \tilde{D}_{61}k_1 + \tilde{D}_{62}k_2 + \tilde{D}_{63}k_3 + \tilde{D}_{64}k_4 + \tilde{D}_{65}k_5 + 2\tilde{D}_{66}k_6 + \lambda_V &= 0 \\ k_1 + k_2 + k_3 + k_4 + k_5 + k_6 + 0 &= VR \end{aligned}$$

The solution to these equations can be expressed in matrix form as:

$$\begin{bmatrix} 2\tilde{D}_{11} & \tilde{D}_{12} & \tilde{D}_{13} & - & - & \tilde{D}_{1N} & 1 \\ \tilde{D}_{21} & 2\tilde{D}_{22} & \tilde{D}_{23} & - & - & \tilde{D}_{2N} & 1 \\ \tilde{D}_{31} & \tilde{D}_{32} & 2\tilde{D}_{33} & - & - & \tilde{D}_{3N} & 1 \\ - & - & - & - & - & - & - \\ - & - & - & - & - & - & - \\ \tilde{D}_{M1} & \tilde{D}_{M2} & \tilde{D}_{M3} & - & - & 2\tilde{D}_{MN} & 1 \\ 1 & 1 & 1 & 1 & 1 & 1 & 0 \end{bmatrix} \begin{bmatrix} k_1 \\ k_2 \\ k_3 \\ - \\ - \\ k_N \\ \lambda_V \end{bmatrix} = \begin{bmatrix} 0 \\ 0 \\ 0 \\ - \\ - \\ 0 \\ VR \end{bmatrix}$$

The matrix equations can be written in condensed form as: $[D][k] = [R]$ (46)

The solution for the unknowns k_i and λ_V is easily obtained by matrix inversion as: $[D][R]^{-1} = [k]$ (47)

The solution to the equations are given by the values of k_i :

The optimized composite wings scaling factor are calculated from k_i as: $s_i = k_i \frac{V_{Base}}{V_i}$ (48)

The optimum z/c distribution is calculated from equation 32 and the corresponding minimum wave drag is obtained from equation 34.

VIII. Including Fuselage and Nacelle Interference Effects

The drag of a wing / body configuration can be calculated using equation 1 with the wing plus body combined area distribution. The area distributions consist of the wing area, A_w plus the body area, A_B distributions:

$$A_t(x, \theta) = A_w(x, \theta) + A_B(x) \quad (49)$$

Substituting equation 49 into equation 1, indicates that the wing plus body drag consists of three components:

$$1. \text{ Drag of the Isolated Wing: } CD_{W_{Wing}} = \frac{1}{2\pi S_{Ref}} \int_0^{2\pi l(\theta)} \int_0^{l(\theta)} A_w''(x, \theta) A_w''(\xi, \theta) \ln|x - \xi| dx d\xi d\theta \quad (50)$$

$$2. \text{ Drag of the Isolated Body: } CD_{W_{Body}} = \frac{1}{S_{Ref}} \int_0^{L_B} \int_0^{L_B} A_B''(x) A_B''(\xi) \ln|x - \xi| dx d\xi \quad (51)$$

$$3. \text{ Wing /Body Interference Drag: } CD_{W_{WBody}} = \frac{2}{2\pi S_{Ref}} \int_0^{2\pi l(\theta)} \int_0^{l(\theta)} A_B''(\xi) A_w''(x, \theta) \ln|x - \xi| dx d\xi d\theta \quad (52)$$

The wing area can be represented as the sum of the areas of the fundamental wing elements.

$$A_w(x, \theta) = \sum_{i=1}^{N_t} A_i(x, \theta) \quad (53)$$

The wing / body interference drag then becomes:

$$CD_{W_{Bint}} = \frac{2}{2\pi S_{Ref}} \int_0^{2\pi} \int_0^{l(\theta)} \int_0^{l(\theta)} A_B''(\xi) \sum_{i=1}^{N_t} A_i''(x, \theta) \ln|x - \xi| dx d\xi d\theta \quad (54)$$

Interchanging the order of summation and integration gives:

$$CD_{W_{Bint}} = \frac{1}{\pi S_{Ref}} \sum_{i=1}^{N_t} \int_0^{2\pi} \int_0^{l(\theta)} \int_0^{l(\theta)} A_B''(\xi) A_i''(x, \theta) \ln|x - \xi| dx d\xi d\theta \quad (55)$$

Define the interference drag between the body and wing element A_i , CD_{wb_i} as

$$CD_{wb_i} \triangleq \frac{1}{\pi S_{Ref}} \int_0^{2\pi} \int_0^{l(\theta)} \int_0^{l(\theta)} A_B''(\xi) A_i''(\xi) \ln|x - \xi| dx d\xi d\theta \quad (56)$$

$$\text{Therefore } CD_{W_{Bint}} = \sum_{i=1}^N CD_{wb_i} \quad (57)$$

The wing / body interference drag is equal to the sum of the interference drags of the body with each of the isolated wing elements.

$$\text{To calculate } CD_{wb_i}, \text{ utilize the identity: } [A_B + A_i]^2 \equiv A_B^2 + 2A_B A_i + A_i^2 \quad (58)$$

$$\text{Consequently: } CD_{wb_i} = CD(A \triangleq A_B + A_i) - CD(A_i) - CD(A_B) \quad (59)$$

The interference drag between the body and wing composite element A_i is obtained by computing the wave drag of the body with the composite wing element and subtracting the isolated body drag, $CD_{W_{Body}}$ and the isolated drag of the composite wing element.

The total wave drag of the wing plus body in terms of the wing composite elements is therefore:

$$CD_W = \sum_{i=1}^{N_t} \sum_{j=1}^{N_t} CD_{ij} \hat{D} + \sum_{i=1}^{N_t} CD_{wb_i} + CD_{W_{Body}} \quad (60)$$

An example of the drag matrix for a six composite element wing is shown if figure 15. The presence of the body adds a single row to the isolated wing drag matrix

	A_1	A_2	A_3	A_4	A_5	A_6
$CD_{W_{body}}$	CD_{wb_1}	CD_{wb_2}	CD_{wb_3}	CD_{wb_4}	CD_{wb_5}	CD_{wb_6}
A_1	\hat{CD}_{11}	$2\hat{CD}_{12}$	$2\hat{CD}_{13}$	$2\hat{CD}_{14}$	$2\hat{CD}_{15}$	$2\hat{CD}_{16}$
A_2		\hat{CD}_{22}	$2\hat{CD}_{23}$	$2\hat{CD}_{24}$	$2\hat{CD}_{25}$	$2\hat{CD}_{26}$
A_3			\hat{CD}_{33}	$2\hat{CD}_{34}$	$2\hat{CD}_{35}$	$2\hat{CD}_{36}$
A_4				\hat{CD}_{44}	$2\hat{CD}_{45}$	$2\hat{CD}_{46}$
A_5					\hat{CD}_{55}	$2\hat{CD}_{56}$
A_6						\hat{CD}_{66}

Figure 15: Example of a Six Composite Element Wing Plus Body Drag Matrix.

The inclusion of the wing / body interference requires only the addition of N+1 additional initial calculations to start the optimization solution.

The total number of individual required element wave drag analyses equals

$$N_{\text{Cal}} = \frac{N^2 + N}{2} + N + 1 \quad (61)$$

The wing plus body drag equation in terms of arbitrary scaling coefficients, s_i is:

$$CD_W = CD_{\text{Body}} + \sum_{i=1}^{N_t} \sum_{j=1}^{N_t} (s_i v_i) (s_j v_j) \frac{CD_{ij}}{v_i v_j} + \sum_{i=1}^{N_t} (s_i v_i) \frac{CDwb_i}{v_i} \quad (62)$$

From before: $\hat{D}_{ij} \triangleq \frac{CD_{ij}}{v_i v_j}$ and $k_i \triangleq s_i v_i$

Let: $Dwb_i \triangleq \frac{CDwb_i}{v_i}$ (63)

The total wave drag equation in terms of the “to be determined” optimization variables, k_i , becomes

$$CD_W = CD_{\text{Body}} + \sum_{i=1}^{N_t} \sum_{j=1}^{N_t} (k_i) (k_j) D_{ij} + \sum_{i=1}^{N_t} (k_i) Dwb_i \quad (64)$$

We will follow the same optimization procedure with Lagrange’s multipliers as for the isolated wing case. The system of linear equations to solve to determine the optimum wing in the presence of a body are:

$$\frac{\partial F}{\partial k_i} = 2D_{ii}k_i + \sum_{j=1, j \neq i}^{N_t} D_{ij}k_j + (Dwb_i + \lambda_v) = 0 \quad (65)$$

Together with the volume constraint equation:

$$\frac{\partial F}{\partial \lambda_v} = k_1 + k_2 + k_3 + k_4 + \dots + k_N - V_R = 0 \quad (66)$$

The solution equations for an example of six composite wing elements plus the body are:

$$\begin{aligned} 2\tilde{D}_{11}k_1 + \tilde{D}_{12}k_2 + \tilde{D}_{13}k_3 + \tilde{D}_{14}k_4 + \tilde{D}_{15}k_5 + \tilde{D}_{16}k_6 + \lambda_v &= -Dwb_1 \\ \tilde{D}_{21}k_1 + 2\tilde{D}_{22}k_2 + \tilde{D}_{23}k_3 + \tilde{D}_{24}k_4 + \tilde{D}_{25}k_5 + \tilde{D}_{26}k_6 + \lambda_v &= -Dwb_2 \\ \tilde{D}_{31}k_1 + \tilde{D}_{32}k_2 + 2\tilde{D}_{33}k_3 + \tilde{D}_{34}k_4 + \tilde{D}_{35}k_5 + \tilde{D}_{36}k_6 + \lambda_v &= -Dwb_3 \\ \tilde{D}_{41}k_1 + \tilde{D}_{42}k_2 + \tilde{D}_{43}k_3 + 2\tilde{D}_{44}k_4 + \tilde{D}_{45}k_5 + \tilde{D}_{46}k_6 + \lambda_v &= -Dwb_4 \\ \tilde{D}_{51}k_1 + \tilde{D}_{52}k_2 + \tilde{D}_{53}k_3 + \tilde{D}_{54}k_4 + 2\tilde{D}_{55}k_5 + \tilde{D}_{56}k_6 + \lambda_v &= -Dwb_5 \\ \tilde{D}_{61}k_1 + \tilde{D}_{62}k_2 + \tilde{D}_{63}k_3 + \tilde{D}_{64}k_4 + \tilde{D}_{65}k_5 + 2\tilde{D}_{66}k_6 + \lambda_v &= -Dwb_6 \\ k_1 + k_2 + k_3 + k_4 + k_5 + k_6 + 0 &= VR \end{aligned} \quad (67)$$

The system of equations are shown below in matrix form.

$$\begin{bmatrix} 2\tilde{D}_{11} & \tilde{D}_{12} & \tilde{D}_{13} & \tilde{D}_{14} & \tilde{D}_{15} & \tilde{D}_{16} & 1 \\ \tilde{D}_{21} & 2\tilde{D}_{22} & \tilde{D}_{23} & \tilde{D}_{24} & \tilde{D}_{25} & \tilde{D}_{26} & 1 \\ \tilde{D}_{31} & \tilde{D}_{32} & 2\tilde{D}_{33} & \tilde{D}_{34} & \tilde{D}_{35} & \tilde{D}_{36} & 1 \\ \tilde{D}_{41} & \tilde{D}_{42} & \tilde{D}_{43} & 2\tilde{D}_{44} & \tilde{D}_{45} & \tilde{D}_{46} & 1 \\ \tilde{D}_{51} & \tilde{D}_{52} & \tilde{D}_{53} & \tilde{D}_{54} & 2\tilde{D}_{55} & \tilde{D}_{56} & 1 \\ \tilde{D}_{61} & \tilde{D}_{62} & \tilde{D}_{63} & \tilde{D}_{64} & \tilde{D}_{65} & 2\tilde{D}_{66} & 1 \\ 1 & 1 & 1 & 1 & 1 & 1 & 0 \end{bmatrix} \begin{bmatrix} k_1 \\ k_2 \\ k_3 \\ k_4 \\ k_5 \\ k_6 \\ \lambda_v \end{bmatrix} = \begin{bmatrix} -Dwb_1 \\ -Dwb_2 \\ -Dwb_3 \\ -Dwb_4 \\ -Dwb_5 \\ -Dwb_6 \\ VR \end{bmatrix}$$

The solution process is exactly the same as for the isolated wing optimization process: equations 46, 47 and 48.

The formulation of the process for optimization in the presence of the nacelles is exactly the same as the process described for including body interference effects.

IX. Adding Local Wing Thickness Constraints

An interesting feature of a linear theory optimization process is that the optimum volume constrained solution may include regions of the wing with vanishingly small or in some instances “negative” thicknesses. This is an indication that in those regions of the wing, volume is accompanied by relatively high wave drag. In essence this is an attempt by the linear theory to “alter” the wing planform. Consequently, in addition to an overall volume constraint, is often necessary to provide the capability to impose local minimum wing thickness constraints.

To accomplish this, we will define a general local depth or area constraint in terms of a desired average thickness/chord ratio at a specific station η_c , and over a portion of the local chord $\Delta x/c$. which is defined as

$$\Delta\psi c = \psi_{aft} - \psi_{fwd} \quad \text{and} \quad 0.0 \leq \psi_{fwd} < \psi_{aft} \leq 1.0$$

The average ToC (in percent) of a base composite element airfoil “i” between the forward station, ψ_{fwd} , and the aft station, ψ_{aft} is:

$$ToC_{elem_i} = \frac{\int_{\psi_{fwd}}^{\psi_{aft}} 2\zeta_i(\psi) d\psi}{\psi_{aft} - \psi_{fwd}} \quad (68)$$

Let $\tau_{ave_{ij}}$, be defined as the local average T/C value, for composite wing “ij” at the constraint spanwise station, η_{con} .

$$\tau_{ave_{ij}}(\eta_{con}) = ToC_{elem_i} \cdot Sy_j(\eta_{con}) \quad (69)$$

This can be converted into a vector relation using the transformation process described by equations 18 and 19

$$\tau v_k \equiv \tau_{ave_{ik,jk_k}} \quad (70)$$

The individual composite average thickness constraints for each of the composite wings vary directly with the scaling factors s_i . The total thickness constraint equation is then

$$\tau_{des} = \sum_k s_k \tau v_k \quad (71)$$

τ_{des} is the desired average T/C over the chordwise interval $\Delta\psi = \psi_{aft} - \psi_{fwd}$ at spanwise station η_{con}

Normalize this equation by the volume ratio of each of the composite wings to obtain

$$\tau des = \sum_k (s_k v_k) \frac{tv_k}{v_k} \quad (72)$$

Define: $\tau cn_k \triangleq \frac{tv_k}{v_k}$

The average thickness constraint equation becomes: $\phi T = \tau des - \sum_{q=0}^{Nt-1} k_q \tau cn_q = 0 \quad (73)$

Following the same procedure as before, we obtain the linear set of equations for determination of the shape of the wing for minimum wave drag in the presence of the body and with both a wing volume constraint and a local average T/C constraint as shown in figure 16.

$$\begin{bmatrix} 2D_{11} & D_{12} & D_{13} & - & - & D_{1N} & 1 & \tau cn_1 \\ D_{21} & 2D_{22} & D_{23} & - & - & D_{2N} & 1 & \tau cn_2 \\ D_{31} & D_{32} & 2D_{33} & - & - & D_{3N} & 1 & \tau cn_3 \\ - & - & - & - & - & - & - & - \\ - & - & - & - & - & - & - & - \\ D_{N1} & D_{N2} & D_{N3} & - & - & 2D_{NN} & 1 & \tau cn_N \\ 1 & 1 & 1 & 1 & 1 & 1 & 0 & 0 \\ \tau cn_1 & \tau cn_2 & \tau cn_3 & - & - & \tau cn_N & 0 & 0 \end{bmatrix} \begin{bmatrix} k_1 \\ k_2 \\ k_3 \\ - \\ - \\ k_N \\ \lambda_v \\ \lambda_T \end{bmatrix} = \begin{bmatrix} -Dwb_1 \\ -Dwb_2 \\ -Dwb_3 \\ - \\ - \\ -Dwb_N \\ VR \\ \tau des \end{bmatrix}$$

Figure 16 System of Equations for Optimization With a Local Thickness constraint

Each local thickness constraint adds an additional row and column to the “D” matrix and an additional row to the “k” and “R” matrices.

The optimum solution is once again obtained as a simple matrix inversion as:

$$[k] = [D][R]^{-1}$$

X. Initial Validation of the FCE Optimization Process

During the early US SST program (circa 1961), Tom Hallstaff of Boeing conducted a supersonic wing optimization study using an early version of an Aerodynamic Influence Coefficient, AIC, panel method.

The objective of the study was to determine the optimum wing spanwise thickness distribution for a delta wing configuration at supersonic speeds. The optimized process was formulated to maximize wing volume for a constant wave drag at the design Mach number = 3.0. The airfoil shape was held constant across the wing span. The thickness to chord ratio for the initial reference wing for the study was constant across the wing span and equal to 2.4%. The study configuration is shown in figure 17.

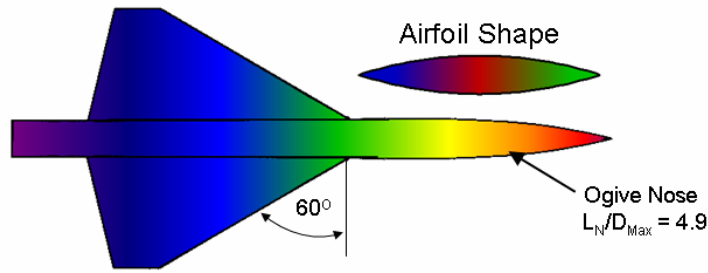


Figure17: Design Optimization Test Case Configuration

The optimized configuration and the reference constant T/C configurations were built and tested in the Boeing supersonic wind tunnel and the Boeing transonic wind tunnel. The design Mach number was 3.0.

Figure 18 contains the “experimental” wave drag measurements for both the baseline and optimized configurations. The “experimental” wave drag was obtained by subtracting calculated fully turbulent flat plate skin friction drag from the test data. The figure also contains recent far field wave drag predictions for each configuration.

The optimized configuration as shown in the figure had an 18.8% increase in wing volume relative to the baseline constant T/C wing body configuration.

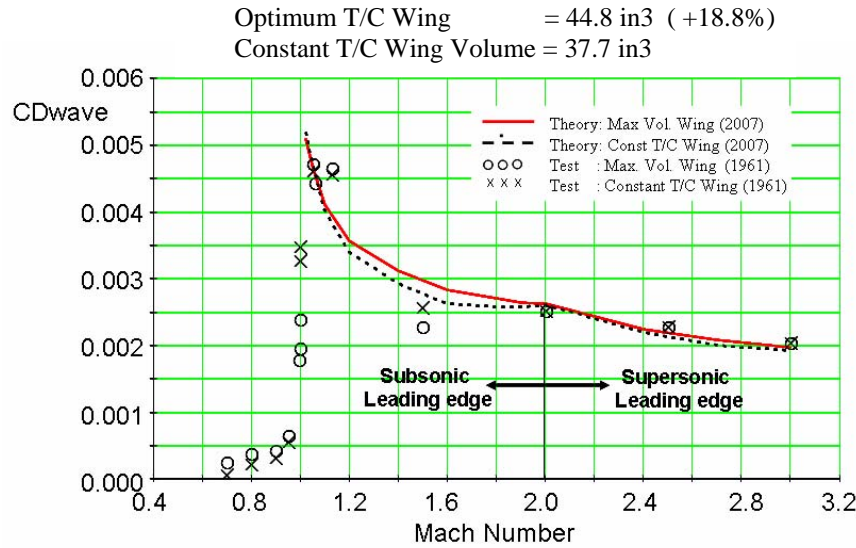


Figure 18 Comparison of Theoretical and Experimental Wing / Body Wave Drag

Above Mach 2.0 the wings had supersonic leading edges in which the Mach number normal to the leading edge was equal to, or greater than Mach 1.0. Above Mach 2.0, the theory and test data indicate that both models had the same wave drag even though the volume of the optimized wing was substantially larger than the baseline wing configuration.

The solution process for minimum wave drag for a given volume, is identical to the solution process for maximum volume for a given wave drag. The only difference is a constant scaling of the wing thickness. For the present study it was decided to optimize the spanwise thickness distribution for a fixed wing volume. The 1961 AIC optimum wing thickness was then reduced to equal the volume of the reference 2.4 % constant T/C wing and the wave drag for the scaled optimum wing was calculated.

For the FCE optimization study, the wing geometry was described by a series of composite wing shapes corresponding to the biconvex airfoil.

The equation for a biconvex airfoil is: $\zeta(\psi) = Sx \cdot C_{1.0}^{1.0}(\psi)$ where $Sx = 2(T_{max}/C)$

The spanwise thickness variation was represented by various orders of Bernstein polynomials, BPO. The total analytic surface was therefore described by the equation:

$$\zeta(\psi, \eta) = \sum_{j=0}^{N_y-1} s_j C_{1.0}^{1.0}(\psi) \cdot Sy_j(\eta) \quad (74)$$

Where s_j are the “to be determined” optimum scaling factors.

N_y corresponds to the selected order of the spanwise Bernstein polynomial, BPO, which was varied from 0 to 6 in the present study to explore convergence of the optimized optimum solution with increasing numbers of composite wing elements.

Figure 19 shows the composite wing elements corresponding to a spanwise BPO = 3 representation.

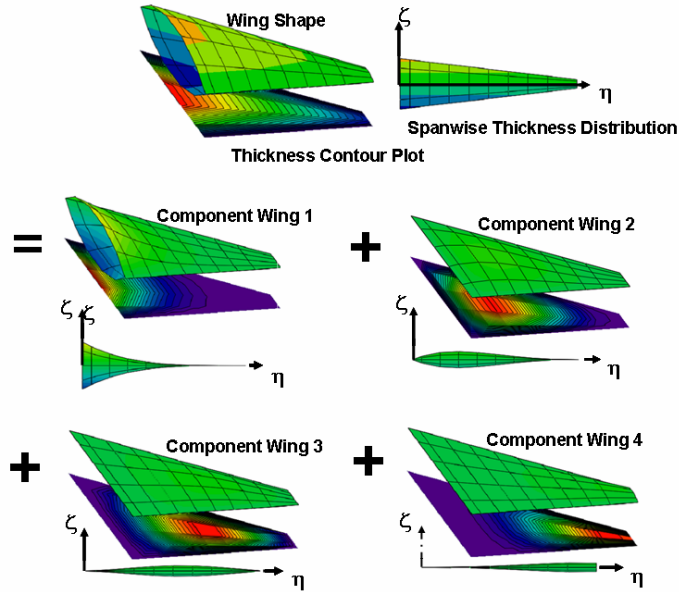


Figure 19: Composite Wing Shapes for Spanwise Bernstein Polynomial of Order 3

Results of the optimization study are shown in Figure 20 for the range of studied composite wing sets corresponding to the various BPO designs.

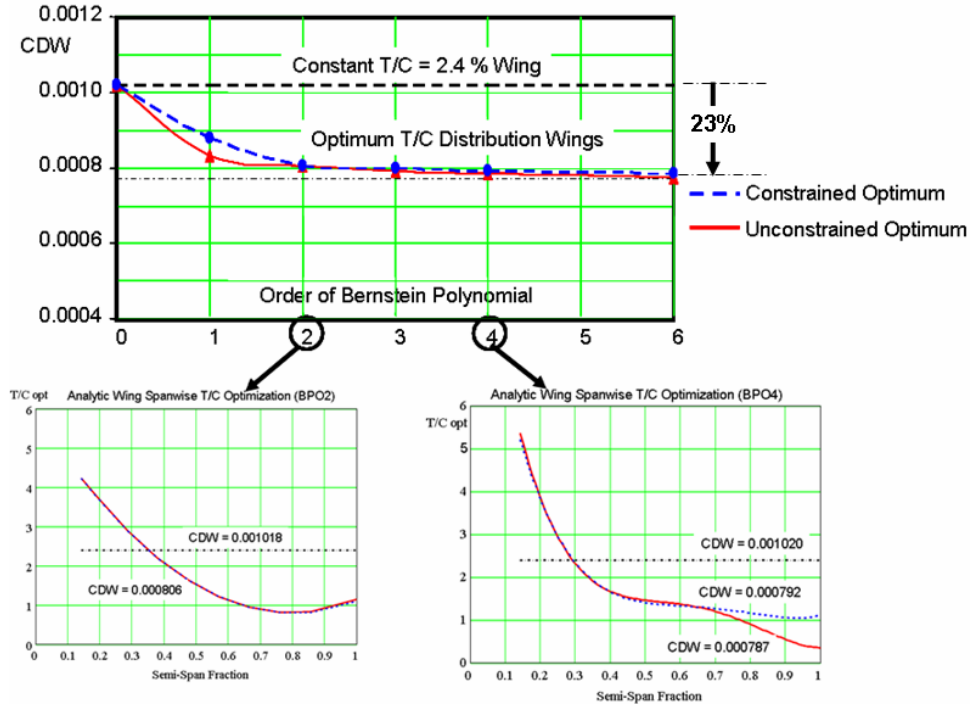


Figure20: Effect of Spanwise BPO Variation on Optimized Wave drag.

The results shown in the figure include constant volume isolated wing optimized designs with and without outboard t/c constraints. The T/C constraints restricted the outboard wing thickness/ chord ratio to a minimum of 2%. The results indicate that the optimum solutions rapidly converged for BPO of 2 and above.

Figure 21 shows comparisons of the FCE BPO = 3 optimized design having 4 variables with the 1961 AIC optimization results that utilized 10 design variables. The results of current and the previous studies are essentially identical.

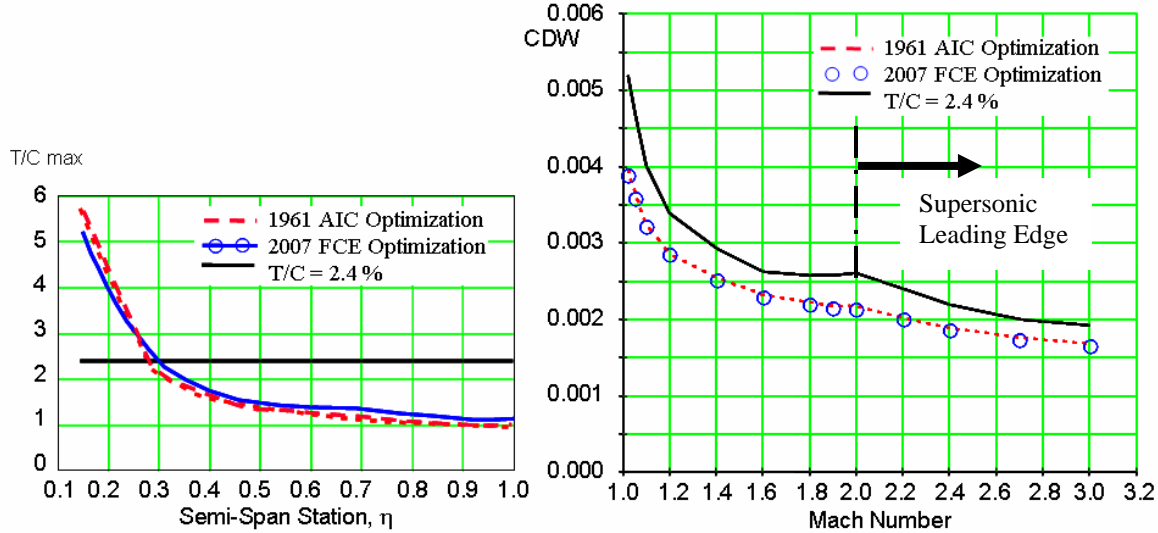


Figure 21 Comparisons of FCE and AIC Wing Optimization Results.

Figure 22 shows the far field analyses wave drag distributions for the optimized designs as a function of the cutting plane angle. The $\theta = 0$ degrees value corresponds to the momentum drag loss in the plane of the wing. $\theta = 90$ degrees corresponds to the momentum loss below the airplane which is often used to calculate sonic boom. Equivalent area plots are also shown for three different cutting plane angles.

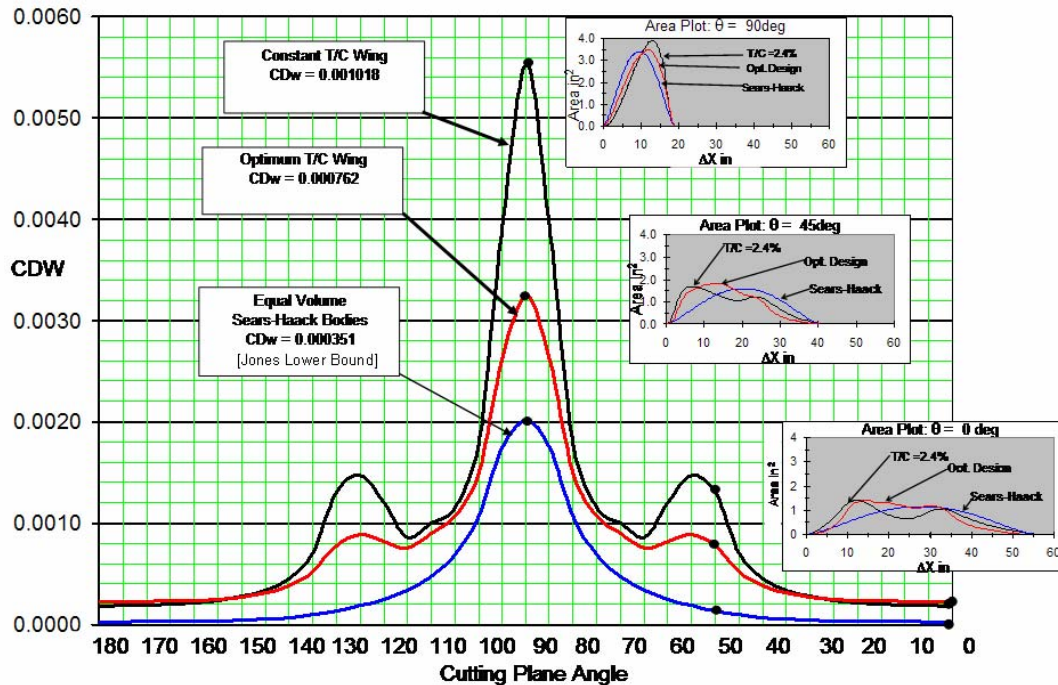


Figure 22 Comparisons of Isolated Wing Far Field Wave Drag Distributions

The theoretical lower bound wave drag is also shown in the figure. This corresponds to every equivalent body shape for all theta angles having the same area distribution as an equivalent volume and length Sears-Haack body. For most planforms this is an impossibility. However, the lower bound drag is often used to serve as a measure of the goodness of a wing design.

XI. Combined Wing Airfoil Shape and Thickness Distribution Optimization

The FCE optimization method together with the CST analytic wing representation technique were utilized to conduct a design optimization study to minimize the wave drag of the arrow wing and ogive / cylinder configuration shown in figure 23.

The wing planform was defined by four parameters:

- Wing Area
- Aspect Ratio (AR = 1.65)
- Taper Ratio ($\lambda = 0.1$)
- Leading Edge Sweep ($\Lambda_{le} = 71.2^\circ$)

The body geometry was defined by a total 5 design parameters:

- Overall Body Length
- Body Maximum Diameter
- Nose Length
- Aft Body Length
- Nose and Aft Body Ogive Distribution Class Function, ND1=ND2=1.0

The overall wing airfoil class function exponents were N1 = 0.5, N2 = 1.0 corresponding to a fundamental round nose with finite boattail angle class of airfoils.

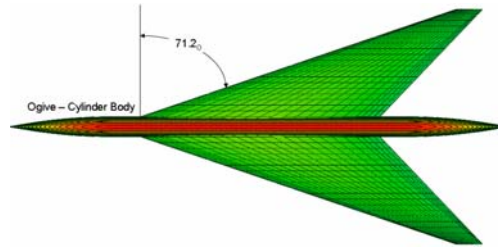


Figure 23: Arrow wing / Body Study Configuration

The analytic wing shape definition for the optimization studies included representation of the basic airfoil shape by a set of four composite airfoils, corresponding to a BPO = 3 representation of the airfoil shape function. The spanwise variation of each of the composite airfoils was described by PBO = 2 representations. The composite airfoil shapes and spanwise variation components are shown in figure 24. This resulted in a family of 12 composite wing geometries corresponding to three spanwise thickness variations for each composite airfoil. The 12 scaling coefficients for the composite wing geometries were the design optimization variables.

The analytic wing definition of the arrow wing shape is therefore:

$$\zeta(\psi, \eta) = \sum_{j=0}^2 S y_j(\eta) \sum_{i=0}^3 s_{ij} C_{1.0}^{0.5}(\psi) S x_i(\psi) \quad (75)$$

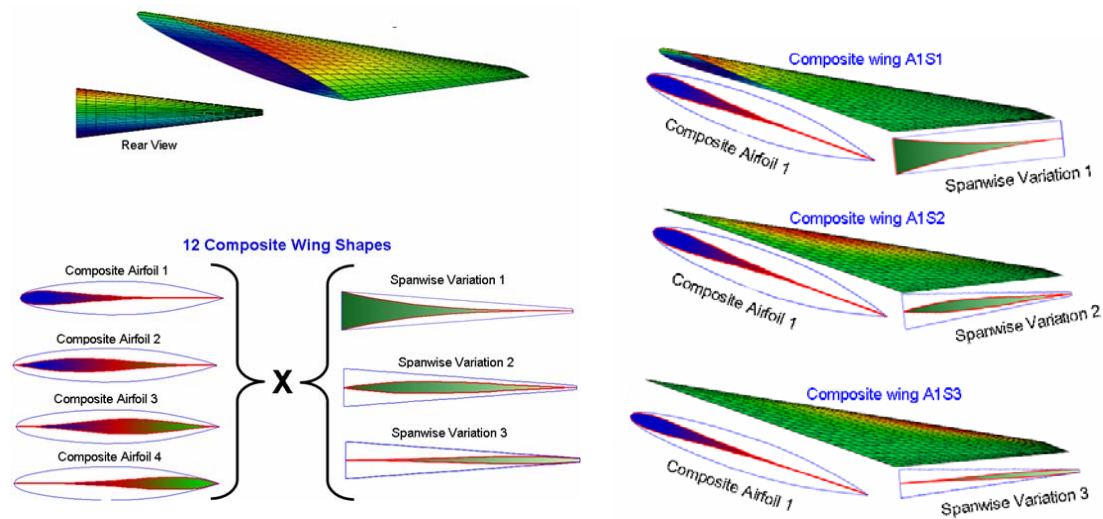


Figure 24: Baseline Wing Analytic Representation Composite Elements

The optimization studies were conducted for two supersonic Mach numbers, Mach = 2.4 and Mach = 3.3.

At Mach 2.4, the wing has a “subsonic leading edge” since the free stream Mach lines are swept less than the wing leading edge. The wing leading edge normal Mach number for this case is equal to 0.773.

At Mach 3.3, the wing has a “supersonic leading edge” since the free stream Mach lines are swept more than the wing leading edge. The wing leading edge normal Mach number for this case is equal to 1.064.

The optimization studies included four cases:

- Case 1: Isolated wing optimization
- Case 2: Isolated wing optimization in the presence of the ogive / cylinder body
- Case 3: Isolated wing optimization with an outboard thickness
- Case 4: Isolated wing optimization with an outboard thickness in the presence of the body

The reference wing for the drag comparisons was an equal volume wing having a constant thickness/chord ratio, T/C, biconvex airfoil. The T/C was equal to 3.45%.

The results for the design Mach number of 2.4 will be initially discussed.

Figure 25 shows the results for of the isolated wing optimization, case 1. The wave drag for the optimum isolated wing is seen to be 29.3% less than the reference configuration. The isolated optimum wing when analyzed with the body is about 23.4% less than the reference wing plus body.

Wing section airfoils across the span are compared with the reference wing airfoil sections. Relative to the reference wing geometry, the optimum airfoil sections have rounded leading edges, the location of the maximum thickness appears to move from aft on the inboard wing to more forward on the outboard wing. The wing trailing edge closure angle for most of the outboard portion of the wing is less than that of the reference wing. These differences will be discussed in greater detail further along in the report.

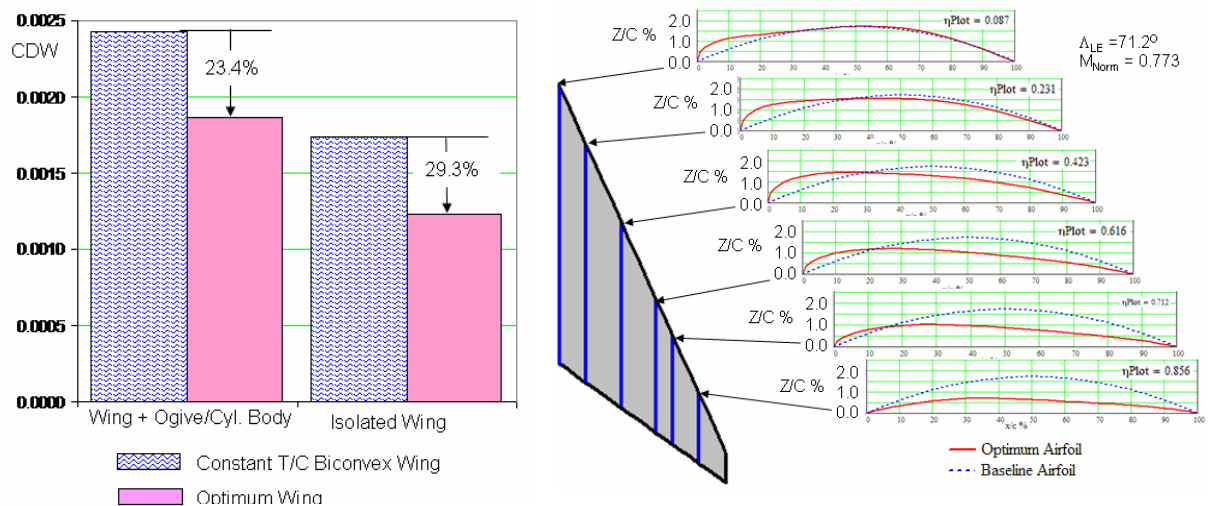


Figure 25: Mach = 2.4 Optimum Isolated Wing Design Constant Wing

The optimum isolated wing thickness distribution becomes rather thin near the wing tip. Consequently a wing thickness constraint was added at 95.2% of the wing span to insure that the wing thickness would never be less than 2% across the wing and the isolated wing was re-optimized with the thickness constraint.

Results of the isolated wing optimization with obtained with the outboard T/C constraint are shown in figure 26.

Restricting the Wing to be no less than 2% thick had extremely small effect on the wave drag of the optimum wing and the optimum wing plus body.

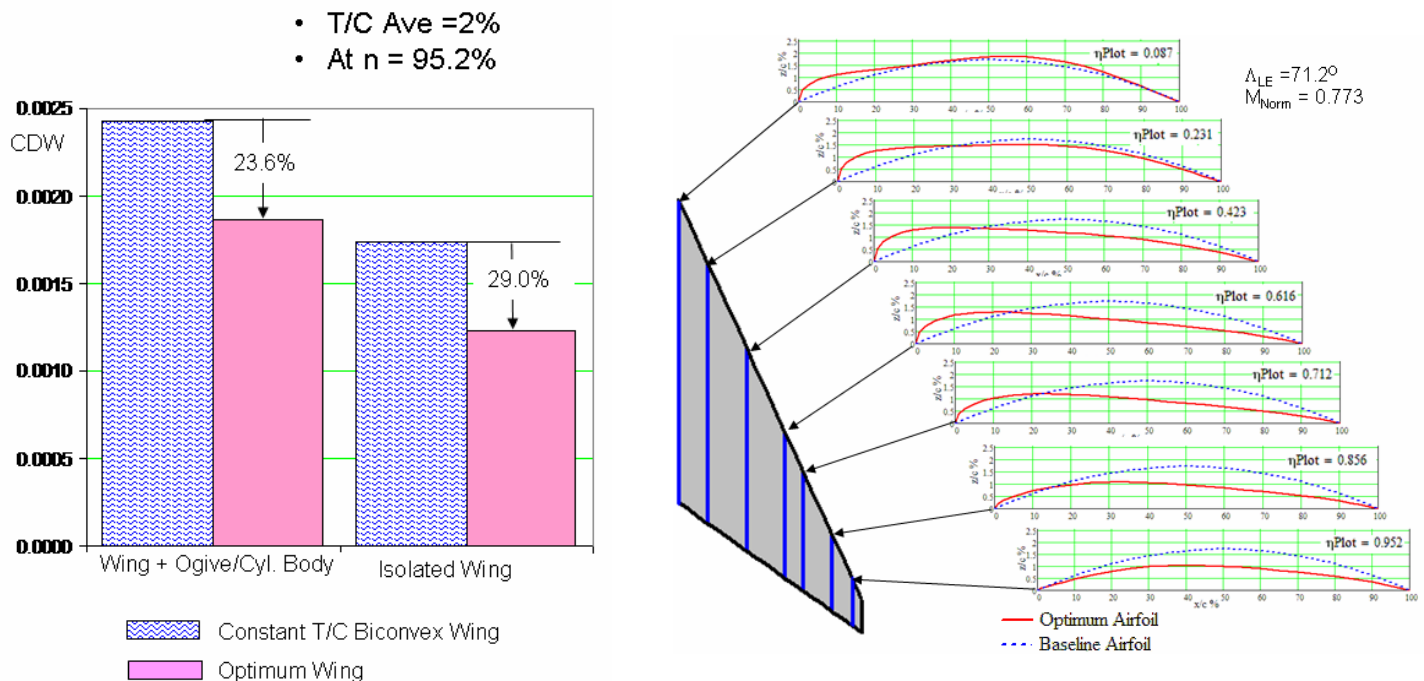


Figure 26: Mach = 2.4 Optimum Isolated Wing Design Constant Wing Volume Plus Outboard Depth Constraint

The results of optimizing the wing in the presence of the body are shown in figure 27.

The isolated wing drag with the thickness constraint is only very slightly higher than the optimum isolated wing, however the combined wing plus body drag is slightly lower (23.6 % lower than the reference wing plus body relative to 23.4% reduction achieved for the case of the isolated optimum wing. In this case the presence of the favorable body interference on wing resulted in an increase in the local wing thickness on the outboard wing near the trip and also at the side of the body. Consequently it was not necessary to include an outboard wing thickness constraint when the body effects were included..

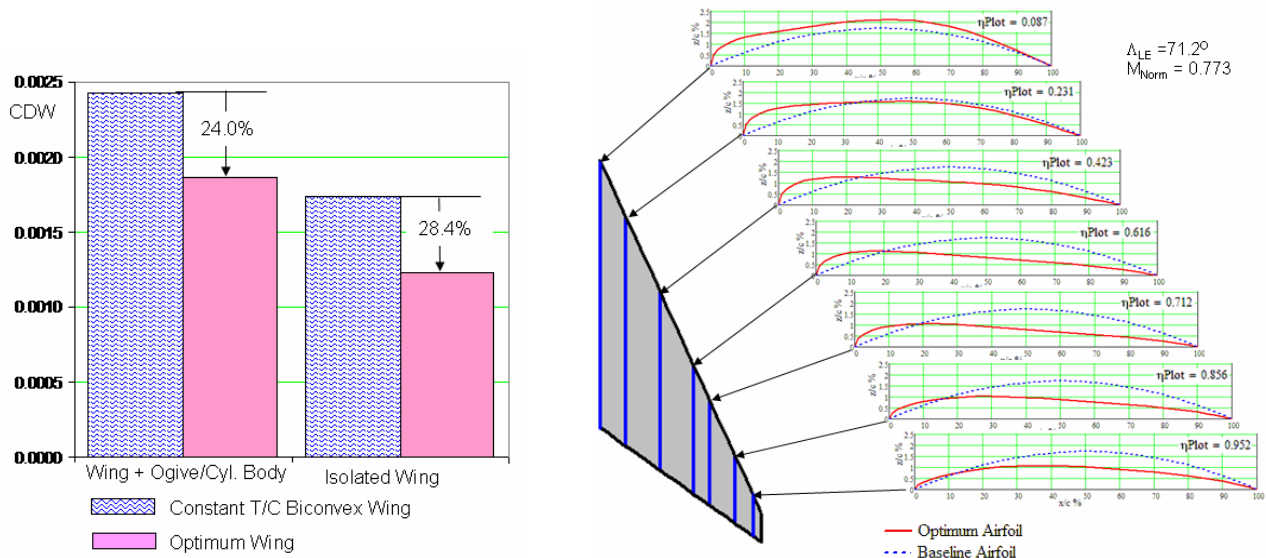


Figure 27: Mach = 2.4 Optimum Wing in the presence of the Ogive/Cylinder Body

Figure 28 through figure 31 contain detailed comparisons of the characteristics of the previously discussed optimized wing designs with the corresponding parameters for the reference wing.

The spanwise variations of the maximum thickness / chord ratio are shown in figure 28.

The optimum isolated wing Tmax/C ratio decreases continually over the entire wing span. This indicates that the nominal drag per unit area is relatively high near the wing tip.

The single outboard wing thickness constraint resulted in a maximum thickness distribution that was greater than 2 % over the entire wing span.

The optimization of the wing in the presence of the body had a rather significant effect on the wing maximum thickness distribution. For this case the spanwise distribution of the maximum thickness over the entire wing was greater than 2%. Hence no thickness constraint was required. Relative to the isolated optimum wing, the wing thickness near the inboard region was increased as well as in the outboard region. The mid-span thickness distribution was decreased. Areas of increased thickness on the wing thickness tend to imply that the body interference effects are favorable in those regions. Conversely, reduction in wing thickness tends to indicate that in those regions the body interference is unfavorable.

The chordwise locations where the maximum thickness occurs are shown in figure 30. The location of the maximum thickness is aft near mid-chord by the side of the body station and rapidly moves forward and remains forward over most of the mid span regions of the wing and then moves aft over the outboard region of the wing. The outboard wing constraint as well as the body resulted in approximately 6% to 8% further forward movement of the maximum thickness location.

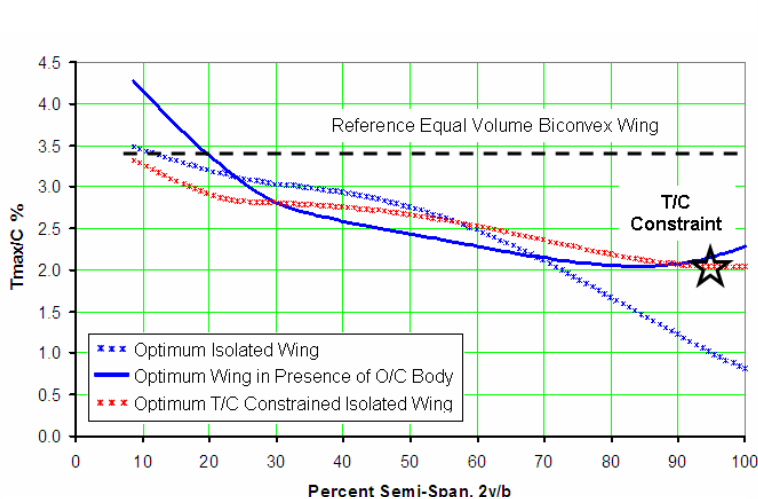


Figure 28: Mach 2.4 Optimum Tmax/C Spanwise Distribution

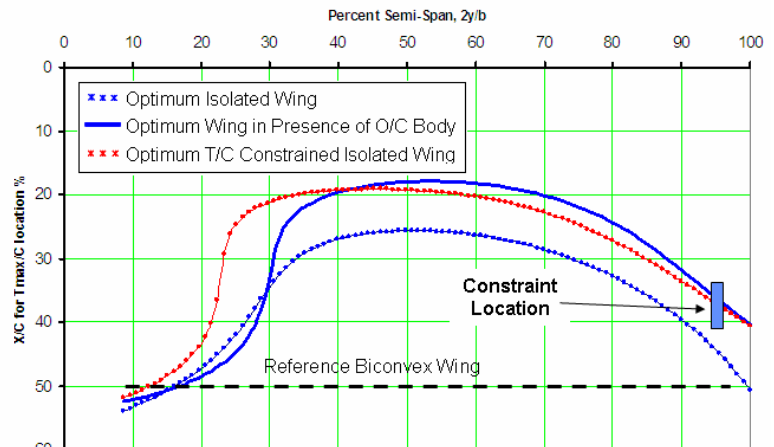


Figure 29: Mach 2.4 Optimum Tmax/C Spanwise Location

The spanwise distributions of the leading edge radius to wing chord ratio, Rle/C for each of the optimized wing designs, are shown in figure 30. The leading edge radius depends not only on the airfoil shape but on the airfoil thickness to chord ratio. In fact the Rle/C varies with $(T_{max}/C)^2$.

Consequently the parameter $\frac{Rle/C}{(T_{max}/C)^2}$ can be considered an indicator of the fundamental leading edge

bluntness of an airfoil. This bluntness parameter for each of the optimized wings is also shown in figure 30.

The study reference wing with a constant T/C biconvex airfoil has a zero radius pointed nose shape nose. Therefore, the leading edge radius and bluntness parameter for an equal volume wing having a constant 3% round nose 65A-Bic airfoil is shown to give an indication of the relative bluntness of the optimized airfoil designs. The 65A-Bic airfoil shape has often been used in preliminary design supersonic transport studies.

All of the optimized wing designs have much greater bluntness than a 65A-Bic airfoil. The outboard wing thickness constraint as well as the presence of the body substantially increased the bluntness of the wing over the entire wing outboard of 20% semi-span.

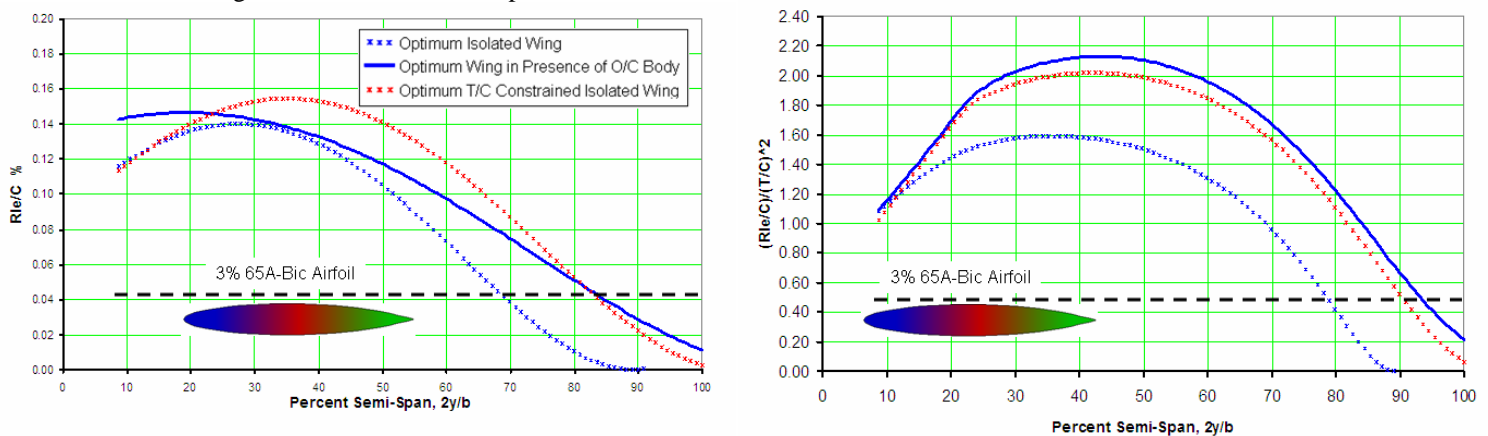


Figure 30: Leading Edge Radius and Nose Bluntness Distribution

The spanwise distributions of the trailing edge closure angles for the optimized wing designs are shown in figure 31. The closure angle depends both on the fundamental shape of an airfoil as well as its maximum thickness to chord ratio. Consequently, the ratio of the closure angle to (T_{max}/C) provides a fundamental measure of the bluntness of the trailing edge of an airfoil. The comparisons in figure 31 indicate that the optimum thickness wings have substantially reduced closure angles over most of the wing. This reduction is primarily due to increased trailing edge sharpness of the optimized designs. This indicates that most likely, a substantial amount of the drag reduction through optimization is due to a decrease in the strength of the trailing edge shock system.

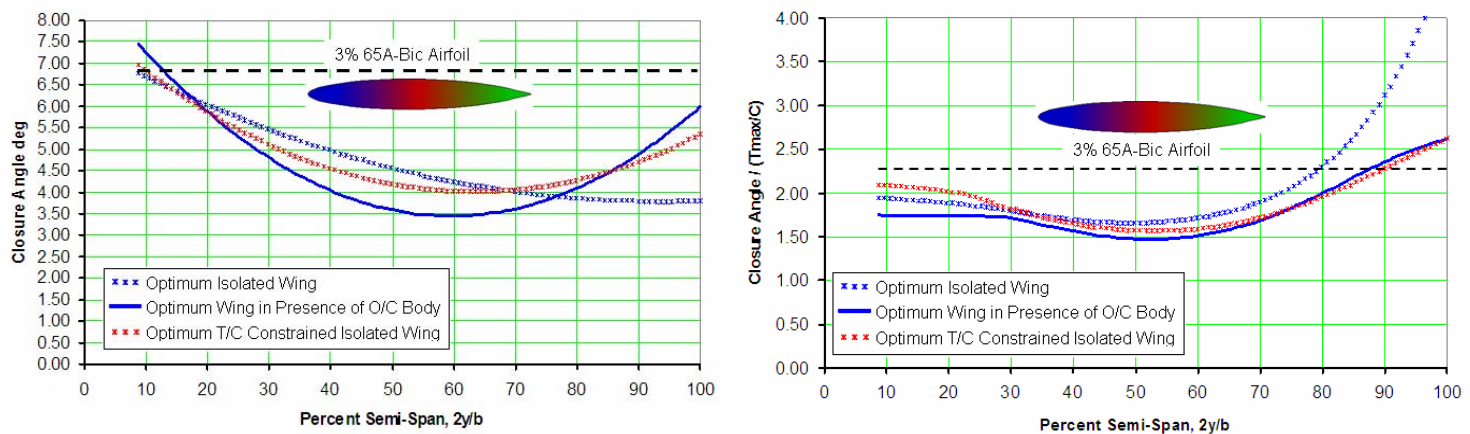


Figure 31: Mach 2.4 Optimum Designs Closure Angle and Trailing Edge Bluntness Distribution

Further insight into the nature of the optimized wing designs can be gained from inspection of the wave drag distribution as a function of the cutting angle as shown in figure 32.

A large source of the wave drag of the reference constant T/C biconvex wing occurs when the cutting plane angle is very close to the sweep of the trailing edge. This is associated with the trailing edge recovery shock. As previously discussed, the optimum wing designs had reduced trailing bluntness which indeed did decrease the wave drag in the region of the trailing edge cutting plane.

It is interesting to note the increased drag of the optimum wings near the $\theta = 90^\circ$ cut. The area distribution associated with this cutting plane is used to calculate the strength of the sonic boom below the airplane flight path. The increased wave drag implies that the optimum wing designs would conceivably increase the strength of the sonic boom.

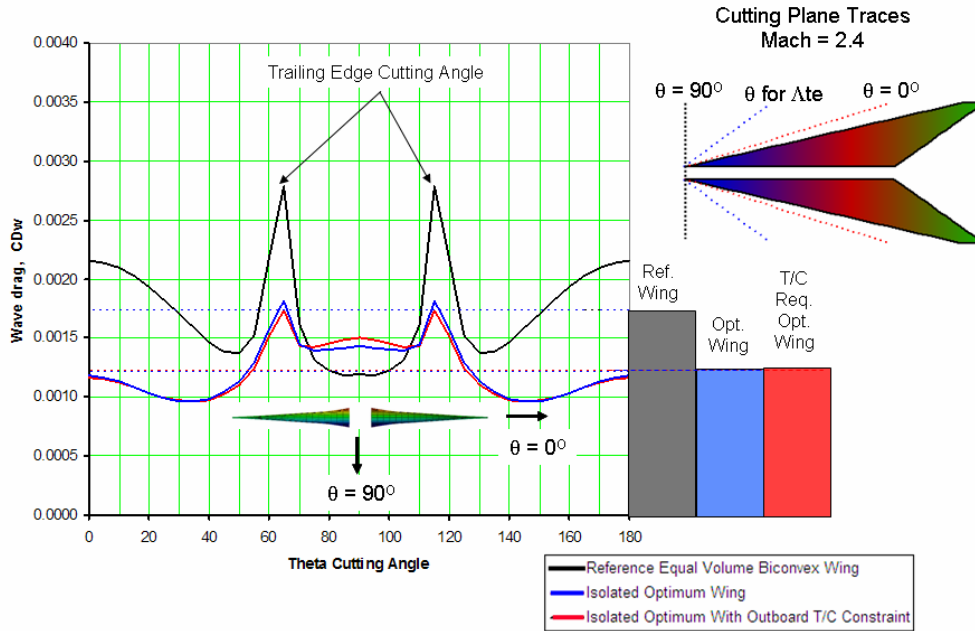


Figure 32: Mach = 2.4 Optimum and Reference Isolated Wings Wave Drag Distributions

The results of the wing optimization conducted at a Mach number of 3.3 are shown in figures 33, through 35.

In these studies, the wing was optimized both with and without the presence of the body, and also with and without an outboard wing T/C constraint. At the design Mach 3.3, the planform has a supersonic leading edge.

The optimized spanwise distributions of T_{max}/C are shown in figure 33. The chordwise locations where the maximum thickness occurred are shown in figure 34.

The isolated optimized wing and the wing optimized in the presence of the body resulted in thickness distributions for which the maximum thickness was much less than 2% of the local chord over most of the outboard part of the wing. Consequently, a single thickness constraint was imposed at 71.1 % of the wing semi-span to insure that T_{max}/C would not be less than 2.0% on the wing. The optimum thickness distributions have similar characteristics in which T_{max}/C is large near the wing root then decreases near mid span and the increases towards the wing tip. These thickness distributions are significantly different than the Mach 2.4 results (figure 28)

The chordwise location of the wings optimized without the T_{max}/C constraint varied from mid chord at the wing root and moved aft to about 70% of the wing chord at about $\frac{3}{4}$ of the wing span and then moved forward to about 40% chord near the wing tip. The wing thickness constraint had a rather significant effect in the chord wise location of the maximum thickness by greatly restricting the chordwise movement of the maximum thickness location across the wing span.

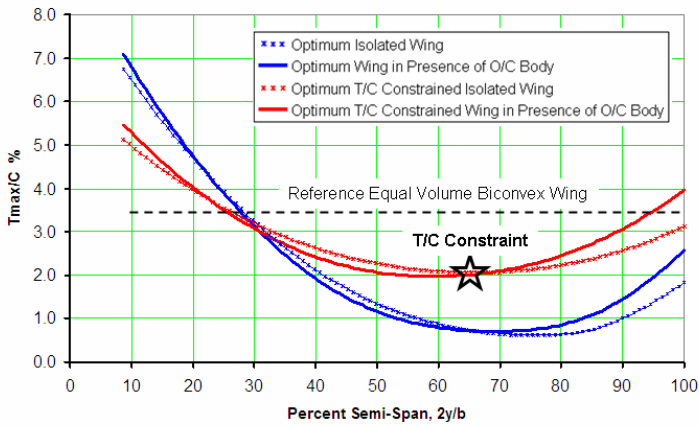


Figure 33: Mach 3.3 Optimum Tmax/C Spanwise Distribution

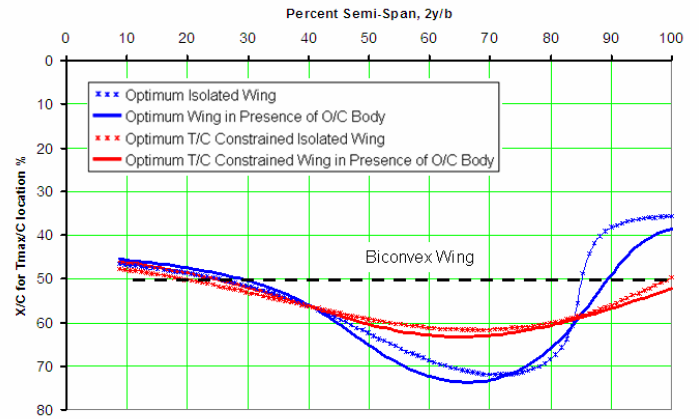


Figure 34: Mach 3.3 Optimum Tmax/C Chordwise Location

Airfoil section shapes for the T/C constrained optimum isolated wing are shown in figure 35: The optimized airfoils have sharp leading edges as would be expected for a supersonic leading edge wing. The chordwise movement of the wing maximum thickness location is readily apparent. The leading edge of the optimum wing has significantly less nose angle relative to the baseline wing. This obviously results in a reduction of the wing leading edge shock system.

These results illustrate the versatility for the CST parametric representation methodology. The composite wing shapes used for both the Mach 2.4 and the Mach 3.3 optimization studies, were developed from the round nose / sharp trailing edge class of airfoils having the class function $C_{1.0}^{0.5}(\psi) = \psi^{0.5}(1-\psi)^{1.0}$.

A sharp leading edge / sharp trailing edge airfoil is fundamentally defined by the class function $C_{1.0}^{1.0}(\psi) = \psi(1-\psi)$. However, as shown in this study, sharp nose airfoils were adequately simulated by with a relatively few composite airfoils derived from the round nose unit airfoil.

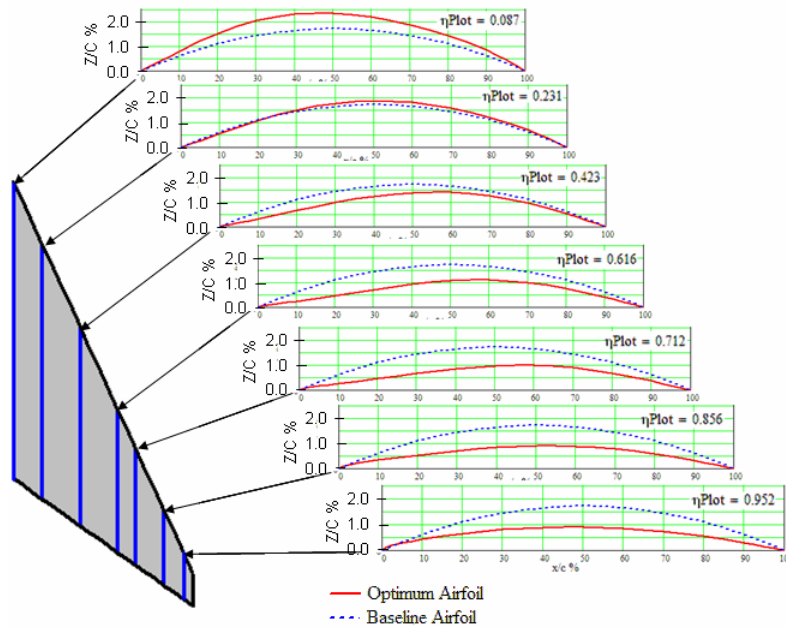


Figure 35: T/C Constrained Isolated Optimum Wing Section Shapes

The wave drags for the optimized isolated wings and the wings optimized in the presence of the body are shown in figure 36. The optimized designs show significant reductions in zero lift wave drag relative to the equal wing volume reference constant T/C biconvex wing configuration.

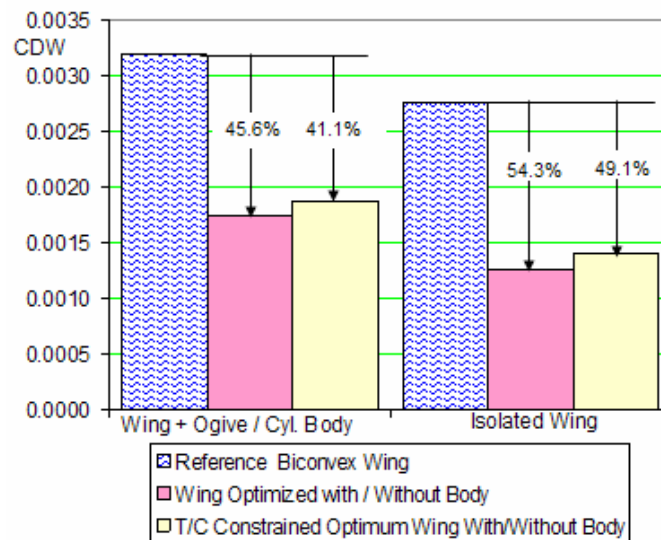


Figure 36: Mach = 3.3 Wave Drag Optimization Results

Figure 37 shows the distribution of the wave drag as a function of the cutting plane angle. It is seen that a large source of the wave drag for the reference wing is associated with the leading edge shock. This indeed was the source of the greatest drag reduction for the optimum wing designs. The T/C constrained optimum slightly increased the drag of the trailing edge shock system.

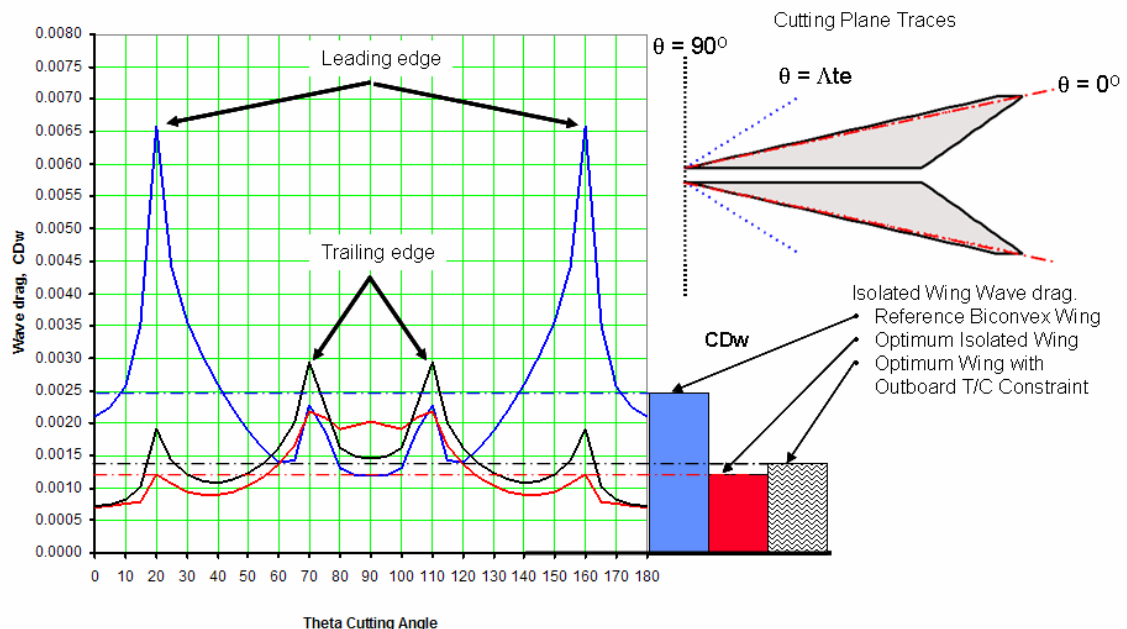


Figure 37: Mach = 3.3 Optimum and Reference Isolated Wings Wave Drag Distributions

The linear theory optimum airfoil shape for a given cross-section area is a biconvex airfoil which is symmetric about the mid chord. The effect of sweep back for a wing with supersonic leading edges, as shown in figure 35 is to move the chordwise location of maximum thickness aft. According to the reverse flow theorem¹⁵, *the drag of a given volume or thickness distribution is the same in forward and reverse flow*. Therefore the optimum solutions for the study sweptback configuration are also the optimum solutions for the equivalent reverse flow swept forward configuration.

The optimum wave drag and the optimum spanwise distribution of T_{max}/C for the swept forward configuration would be the same as in figures 36 and 33 respectively. However the chordwise location of the maximum thickness would move forward of the mid span location as shown in figure 38.

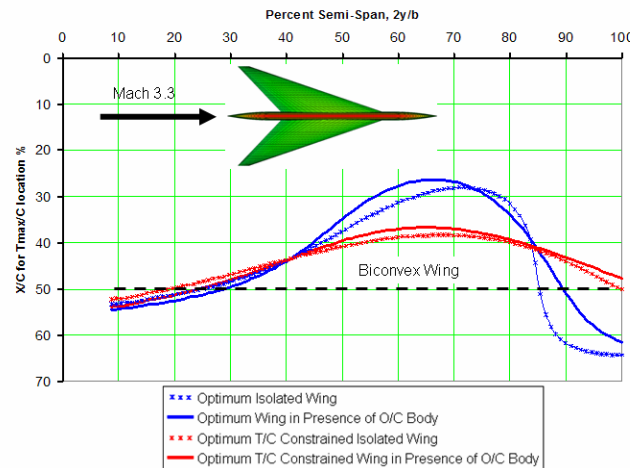


Figure 38: Mach 3.3 Swept Forward Wing Optimum T_{max}/C Chordwise Location

XII. FFWD and FCE Paradox

The Far-Field Wave Drag, FFWD method is based on the fundamental assumption that the control volume for the drag calculation process is “so far” from the wing and body that the details of the configuration shape do not matter. However, the FCE optimization method that utilizing the FFWD method determines how to shape the wing geometry so that it does matter

XIII. Summary and Conclusions

- The good agreement between linear theory predictions of the cruise drag polars for supersonic transport configurations justifies the continued use of linear theory methods in the preliminary design development and trade studies both individually and in conjunction with non-linear CFD methods.
- A new method (FCE) for optimizing zero lift wave drag of supersonic configurations utilizing the “CST” universal parametric geometry method was presented.
- The FCE methodology also allows easy and efficient exploration of the effects of various design constraints on minimum zero lift wave drag.
- The integration of the FCE optimization with the new CST geometry representation technique has been shown to provide a simple and an effective systematic and powerful design optimization process.
- The CST analytic representation methodology provides a very large design space of analytic wing representations with a relatively few number of design variables.
- The concept of the CST analytic wing definition was shown to be an effective geometric representation method for design optimization.

References

1. Kulfan, B.M, and Bussoletti, J.E., "'Fundamental Parametric Geometry Representations for Aircraft Component Shapes". AIAA-2006-6948, September 2006
2. Kulfan, B. M., "A Universal Parametric Geometry Representation Method – CST", AIAA--2007-0062, Jan 2007
3. Kulfan, B. M., "Recent Extensions and Applications of the "CST" Universal Parametric Geometry Representation Method", AIAA-2007-7709, Sept. 2007
4. Wilcox, D.C., TURBULENCE MODELING FOR CED, DCW Industries, La Canada, California, 2006, pp 3
5. Kulfan, R.M. and Sigalla, A., "Real Flow Limitations in Supersonic Airplane Design:", AIAA-78-147, Jan. 1978
6. Kulfan, B. M., Reynolds Numbers Considerations for Supersonic Flight", AIAA-2002-2839, Jun 2002
7. Kulfan, B. M., "Assessment of CFD Predictions of Viscous Drag", AIAA 2000-2391, June 2000
8. Harris, R. V., Jr., "An Analysis and correlation of Aircraft Wave Drag", NASA TMX 947, Oct. 1961
9. Middleton, W. D., and Lundry, J. L., A Computational System for Aerodynamic Design and Analysis of Supersonic Aircraft. NASA CR-2715, March 1976.
10. Kulfan, B. M., "Fundamentals Supersonic Wave Drag", Fourth International Conference on Flow Dynamics, Sendai, Japan, September 2007
11. Lomax, H. and Heaslet, M. A., "A Special Method for Finding Body Distortions that Reduce the Wave Drag of Wing and Body Combinations at Supersonic Speeds", NACA RM A55B16, May 1955
12. Lomax, H. and Heaslet, M. A., "Recent Developments in the theory of Wing-Body Wave Drag", J. Aeronautical Sci., vol. 23, no 12, pp 1061-1074, 1956
13. Lomax, H., "The Wave Drag of Arbitrary Configurations in Linearized Flow as Determined by Areas and Forces in Oblique Planes.", NACA RM A55A18, 1955
14. Jones, R.T., "Theory of Wing-Body Drag at Supersonic Speeds", NACA RM-A53H18a, Sept. 1953
15. Ashley, H. and Landahl, M., AERODYNAMICS OF WINGS AND BODIES, Addison-Wesley Publishing Company, INC., Reading, Massachusetts, 1965, pp 196.